

Reply to Referee #1

We thank the reviewer for the insightful and constructive comments. In the following, we reply point by point on the reviewer's comments. They are shown in italic, our replies are in plain red and manuscript modification that we will make are in blue.

5

The manuscript titled “Micromechanical modeling of snow failure” by Bobillier et al. reports the setup and the results of numerical DEM models aiming at studying the failure of weak snow layers. The paper is based on the fact that complex and detailed numerical models are extremely time-consuming. On the contrary, it is possible to build simplified models that are able to catch the main characteristics of the investigated material. In the proposed approach, such models are constituted by

10 *different layers of spherical particles. The approach is original and interesting results can be obtained from such numerical setup. The authors “tuned” particle properties by simulating real experiments. This approach is commonly used in other engineering disciplines.*

In addition, they predicted the behavior of such complex material under particular stress conditions, say, pure traction, for which no experimental pieces of evidence are present. Referring to this last point, the possibility of “extrapolating” the

15 *behavior to something that is hard to replicate in a laboratory has to be further discussed in detail and the limitation of the approach must be clearly stated.*

In addition, there are some points that are not clear and must be detailed.

We amended our manuscript to clarify some parts that were unclear to the reviewer and more thoroughly discuss the limitations of the model and how the results can be generalized.

20 **1 P.2, L.6: to which properties do the authors refer with “and possibly other ones”?**

We added examples of other snow properties that can be related to the dynamics of crack propagation such as slab porosity, weak layer failure envelope, weak layer elasticity, microstructure (P.2, L.6):

However, no theoretical framework exists that describes how these mechanical properties and possibly other ones such as weak layer failure envelope, weak layer elasticity or microstructure relate to the dynamics of crack propagation at the slope

25 scale.

2 Referring to the contact model (P.3), it is not clear when the contacts are activated and when not. In other words, it is possible that new contacts form during the test, or not?

Thank you for this remark. Once a bond breaks, only particle frictional contact occurs and no new bonds are created (i.e no sintering occurs). This assumption is motivated by the fact that the strain rate is large and the time scale is seconds during a PST experiment. We explicitly mentioned that we do not expect sintering (P.3, L12).

In addition, a more detailed description of the contact model is given in the manuscript with the following figures (a, b).

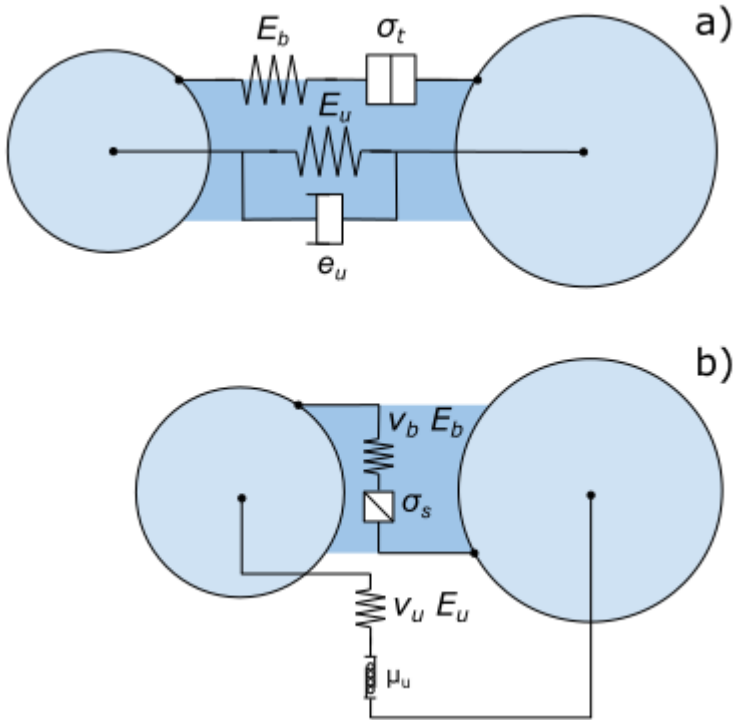


Figure a: Representation of the PFC parallel bond model (PBM) used in the simulations. a) Normal mechanical parameter bond and unbonded, where E_b represents the bond elastic modulus, σ_t the tensile strength, E_u the contact elastic modulus and e_u the restitution coefficient. b) Shear mechanical parameter bond and unbonded, where E_b represents the bond elastic modulus, σ_s the shear strength, E_u the contact elastic modulus, v_b the bond Poisson's ratio and μ_u the friction coefficient.

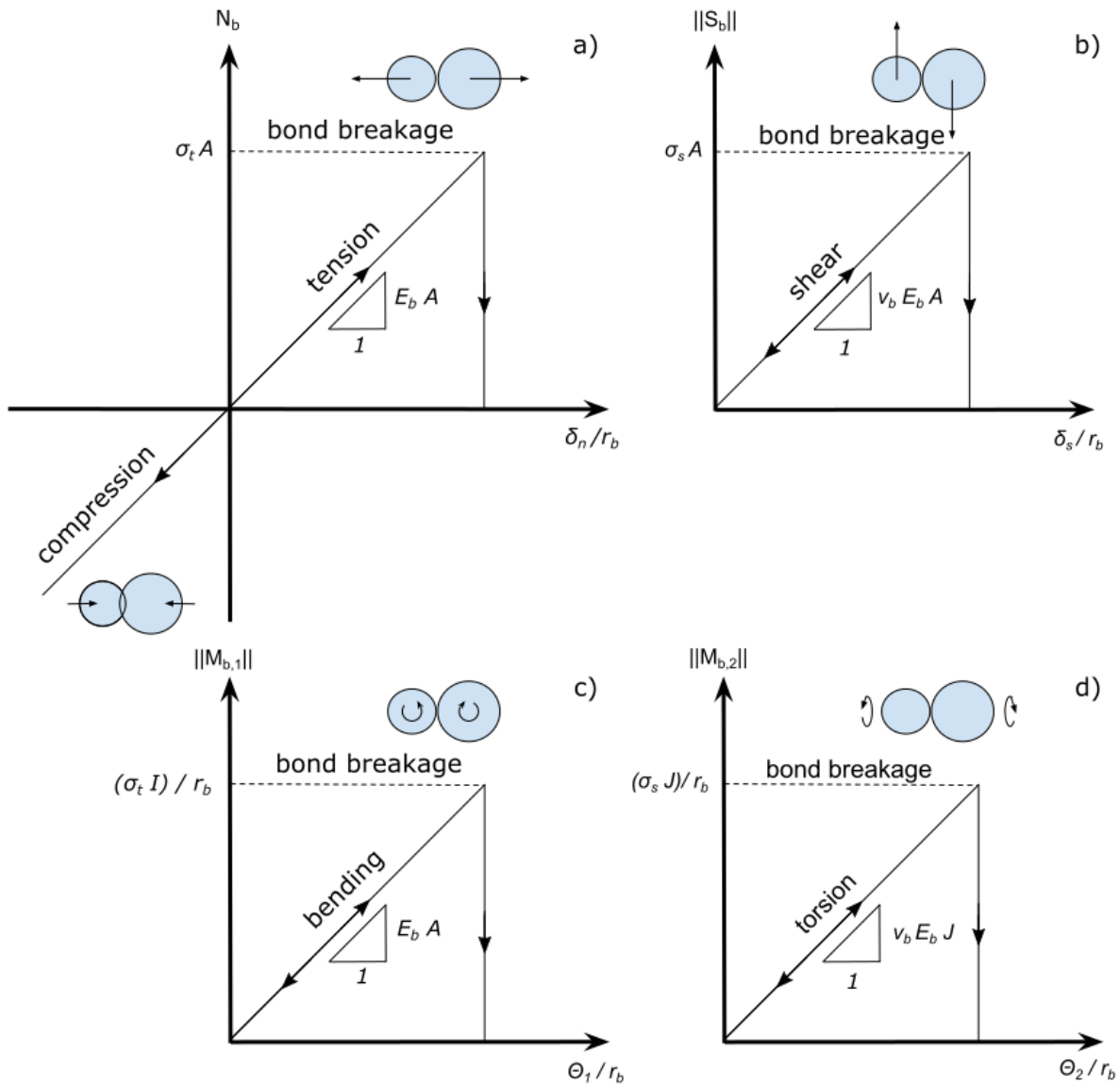


Figure b: Representation of the bonded behavior of PBM used in the simulations. (a) Bond normal force N_b as a function of the normal interpenetration δ_n scaled by the bond radius r_b . (b) Bond shear force $\|S_b\|$ as a function of tangential interpenetration δ_s scaled by the bond radius r_b . (c) Bond-bending moment $\|M_{b,1}\|$ as a function of bending rotation θ_1 scaled by the bond radius r_b . (d) Torsion moment $\|M_{b,2}\|$ as a function of twist rotation θ_2 scaled by the bond radius r_b .

3 **P.3 L.15: scaling the size of the layer through homothetic transformation does allow to state that the mechanical properties are conserved? short but detailed study on scaling laws would be appreciated.**

5 Performing simulations of weak layers of different thickness generated through homothetic transformation shows the same mechanical results (see figures c, d). The bond strength and elastic modulus are scaled such that the macroscopic mechanical behavior becomes almost exactly the same for different values of weak layer thickness (see figures c, d). This is clarified in a section that is added to the supplementary material. The equation to characterize macroscopic properties can be written as:

$$E_{wl\ macro} = (\beta_0 + \beta_1 E_{particle}) / \left(\frac{h_{wl\ ref}}{h_{wl}}\right)$$

$$\sigma_{wl\ macro}^{th} = (\gamma_0 + \gamma_1 \sigma_{bond}^{th}) / \left(\frac{h_{wl\ ref}}{h_{wl}}\right)$$

Where $h_{wl\ ref} = 3\text{cm}$ and h_{wl} correspond to the new weak layer thickness.

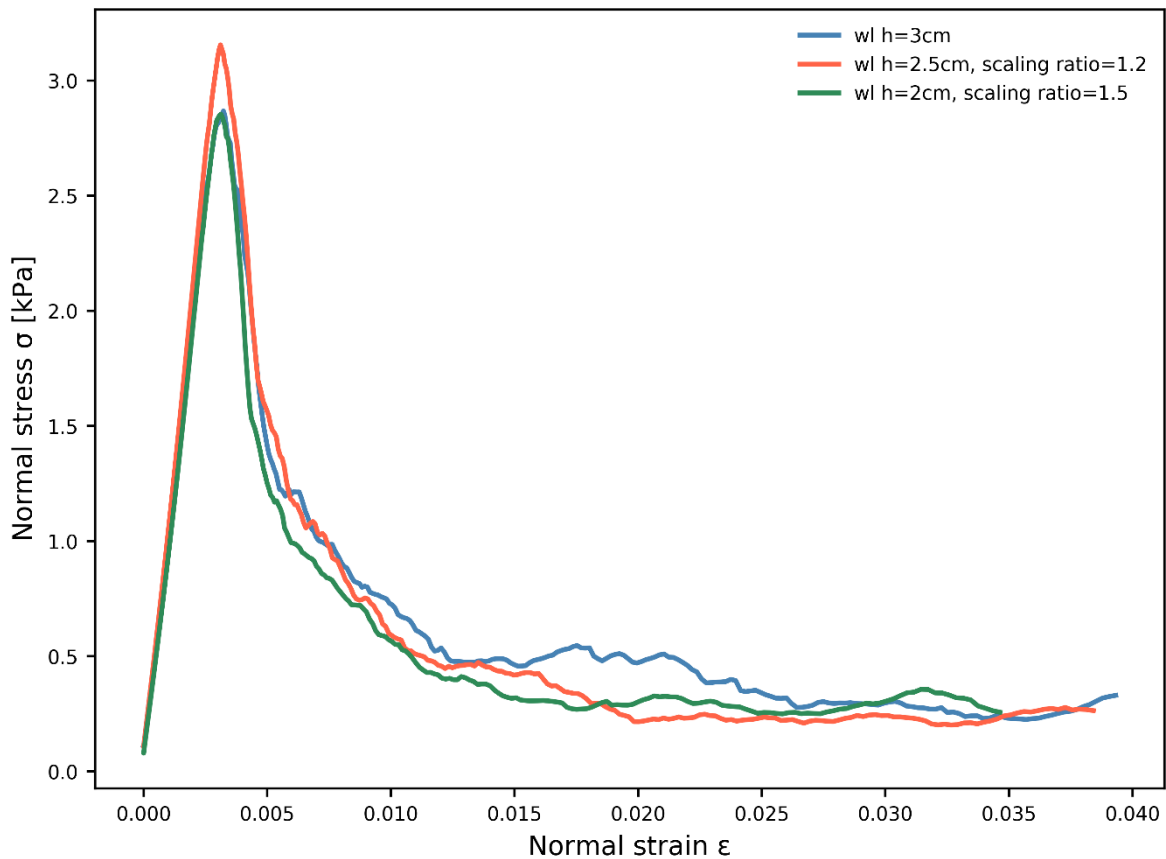


Figure c: Stress-strain curves for weak layers of different thickness (colors) under load-controlled compression. The blue line shows the reference weak layer with a thickness of 3 cm.

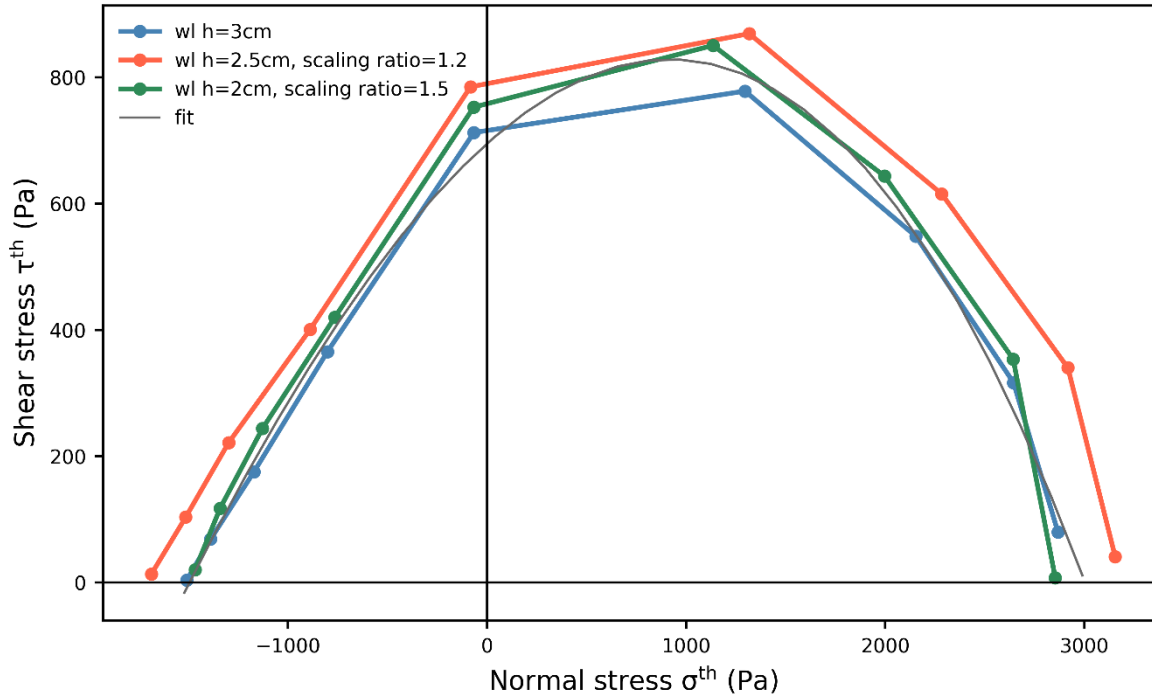


Figure d: Failure envelopes for weak layers with different thicknesses (colors) and fits based on equation (9).

5 **4 P.3 L.25: a lot of attention is given to the density. Why? It seems that the results are not density-dependent**

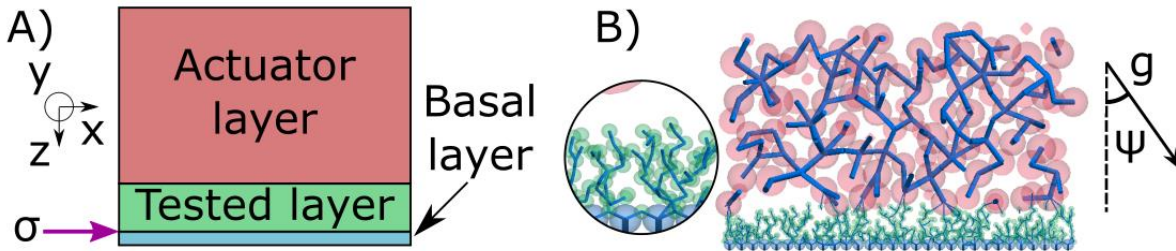
In a real snowpack, snow density is a very important parameter, as many mechanical properties scale with density (e.g. Shapiro et al. 1997, van Herwijnen et al., 2016). Snow properties such as $\sigma_{slab\ macro}^{th}$ or $E_{slab\ macro}$ are thus often defined as function of mean slab density. However, slab density directly relates to the load on the weak layer, which influences crack propagation propensity and thus slab avalanche release. The density and the thickness of the slab will determine the load. If the stress state given by this load is outside of the failure envelope of the weak layer, failure can occur. Here, a lot of attention was given to the evaluation of the failure envelope, which defines the critical load. In our simulations, as you correctly mention, weak layer density does not play a crucial role.

5 **P.4 L.5: the authors assumed that bond strength and particle elastic modulus are independent. Is this consideration supported by data, observations, previous researches, or is it a hypothesis?**

In some materials strength and elastic modulus are related, while in other materials both properties are not related. For snow, it remains unclear if those two properties are related. Our goal was to independently control both parameters in order to have a precise control on the macroscopic elastic modulus and macroscopic strength of the snow

6 **P.4 L.20: it is not clear the test setup. It seems that the density of the actuator layer is rapidly increased to simulate a normal vertical pressure. Why we should expect shear strains into the weak layer?**

We improved Figure 1 in the manuscript to more clearly illustrate the test setup (see figure e) (P.3, L.19).



10 **Figure e: A) Coordinate system and diagram of the setup consisting of the basal layer (blue), the tested layer, in this case a weak layer, (green) and the actuator layer (red). The violet arrow points to the interface between basal and tested layer where the stress is measured. B) slice of a generated system consisting of a slab layer (large red particles) and a porous weak layer (small green particles). A zoom of the weak layer is shown in the circle. The lines represent bonds between particles. Applied gravity is defined on the right where ψ is the loading angle.**

15 **The stress on the weak layer is increased by increasing the density of the actuator layer. By changing the gravity, mixed-mode loading is simulated. Through this change in the angle of gravity, the tested layer is under both shear and normal stresses. This is clarified in the manuscript (P.4, L.24).**

7 **Referring to the characterization of macroscopic properties, the authors performed a Latin hypercube sampling on the values of the elastic modulus of the particle and the strength of the bond and obtained the macro-properties of the slab. Many issues arise: why in Figure 2a only 9 simulation points appear, while the authors have performed 100 simulations? Are those points related to a particular value of σ_{bond}^{th} ? Are the values of coefficients β_0 : feasible/realistic? Please add the units of measure to β_0 and γ_0 .**

25 **Thanks for this remark. We performed 9 x 9 simulations (81 simulations) for the weak layer (Fig. 3) and 10 x 10, 100 simulations for the slab layer (Fig. 2). This is clarified in the manuscript (P.7, L.6). In Figure 2a, each blue dot represents the mean value of the macroscopic elastic modulus for a fixed $E_{particle}$ and ten σ_{bond}^{th} values (as explained in the caption). A qualitative comparison with data presented by Shapiro et al. (1997) suggests that the values we used are realistic for slab and weak layers. The goal of the layer characterization is to show that the macroscopic properties (E_{macro} , σ_{macro}^{th}) can be**

controlled in a range that is typical for snow. The units of β_0 and γ_0 are Pascal (Pa), which we added in the manuscript (P.7, L.1, L.4, L.10, L.13).

8 ***Referring to the mechanical behavior of layers, it is necessary to define what a failure is. Failure in tension is different from failure in compression or in shear. Referring, for example, to tension tests, how such tests were performed? Have the results of tension tests been compared with tests on real snow? In general, synthetic models are able to “interpolate” rather than “extrapolate”.***
5

In our simulations, mixed-mode loading is applied by changing the angle of gravity. We agree that this was not clearly stated. We revised the manuscript to clarify this point (P.4, L.23). Hence, the identification or definition of failure does not depend on the mode of loading. Failure is simply identified as the point of maximum shear or normal stress. This point precedes the onset of softening (see Figure below). We clarified this as well in the manuscript.
10

Tension tests were simulated with a negative gravity ($\psi = 180^\circ$). For tension test results we are in the upper range of the tensile strength values reported by Sigrist (2006). However, we can calibrate our microscopic properties to get the macroscopic properties we want.

9 ***P.8 L.11: Which is the meaning of “shear acceleration”?***

15 Thanks for this remark. We agree that the term shear acceleration was not very adequate and we changed it to “**tangential acceleration**” in the manuscript (P.8, L.26). This tangential acceleration is the 2nd derivative of the tangential displacement.

10 ***Referring to the failure envelope reported in Eqn. (9), what σ^{th} does represent? Can the failure envelope be used in a real snowpack on a real slope? In addressing this issue, the authors must consider the fact that their tests were performed in unconstrained lateral conditions, different from boundary conditions that can be observed in a continuous layered snowpack.***
20

Thank you very much for noticing this omission of defining σ^{th} and τ^{th} . σ^{th} represents the fitted normal strength and τ^{th} the fitted shear strength. This is modified in the manuscript (P.9, L.9). Concerning the second aspect on the confinement and real slopes, we checked that unconfined and confined loading conditions yield the same results for weak layer behavior. This finding is due to the large porosity (80%) of the weak layer (see figure f). We added this figure to the supplementary material.

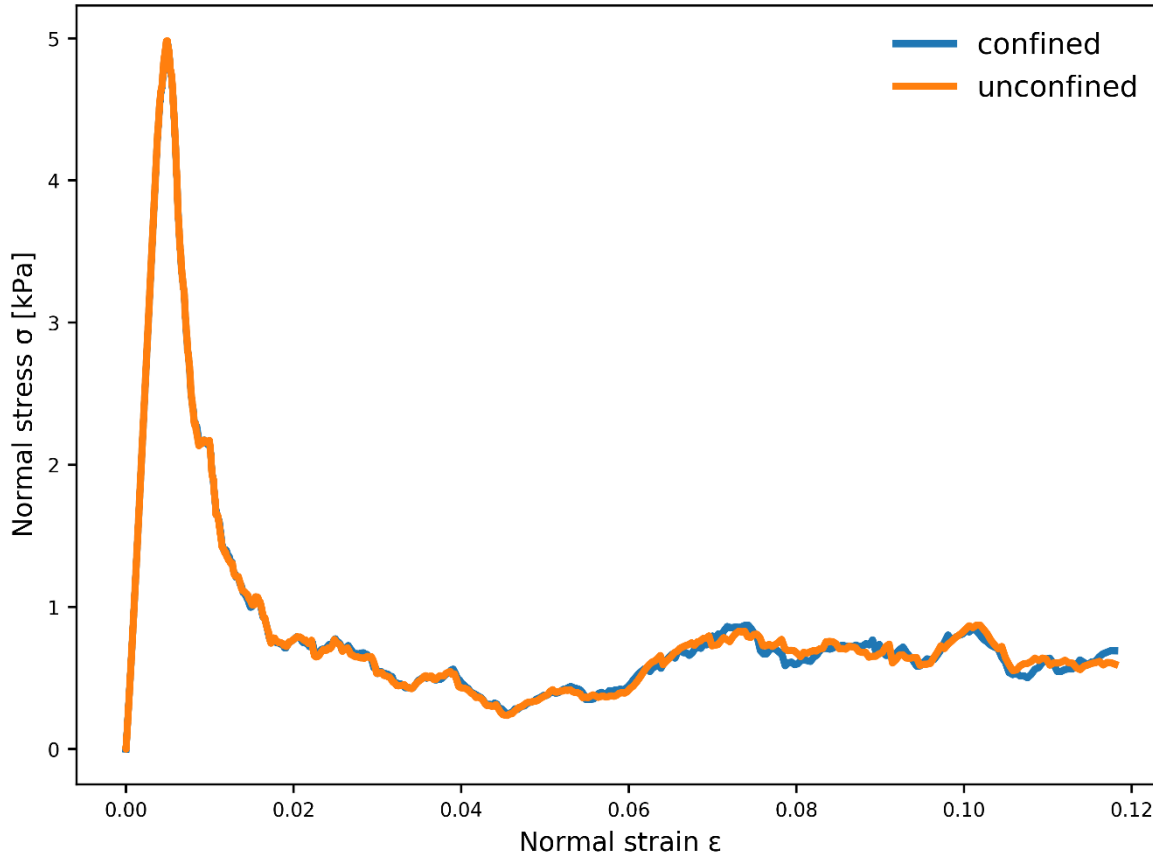


Figure f: Weak layer behavior under load-controlled compression ($E_{particle} = 1 \text{ MPa}$ and $\sigma_{bond}^{th} = 5 \text{ kPa}$). The blue line shows the normal stress during confined test and the orange line during unconfined test conditions.

11 *As stated in the introduction, the failure of snow slabs depends on many parameters, such as the fracture energy.*
 5 *Have the authors considered this important parameter in their simulations?*

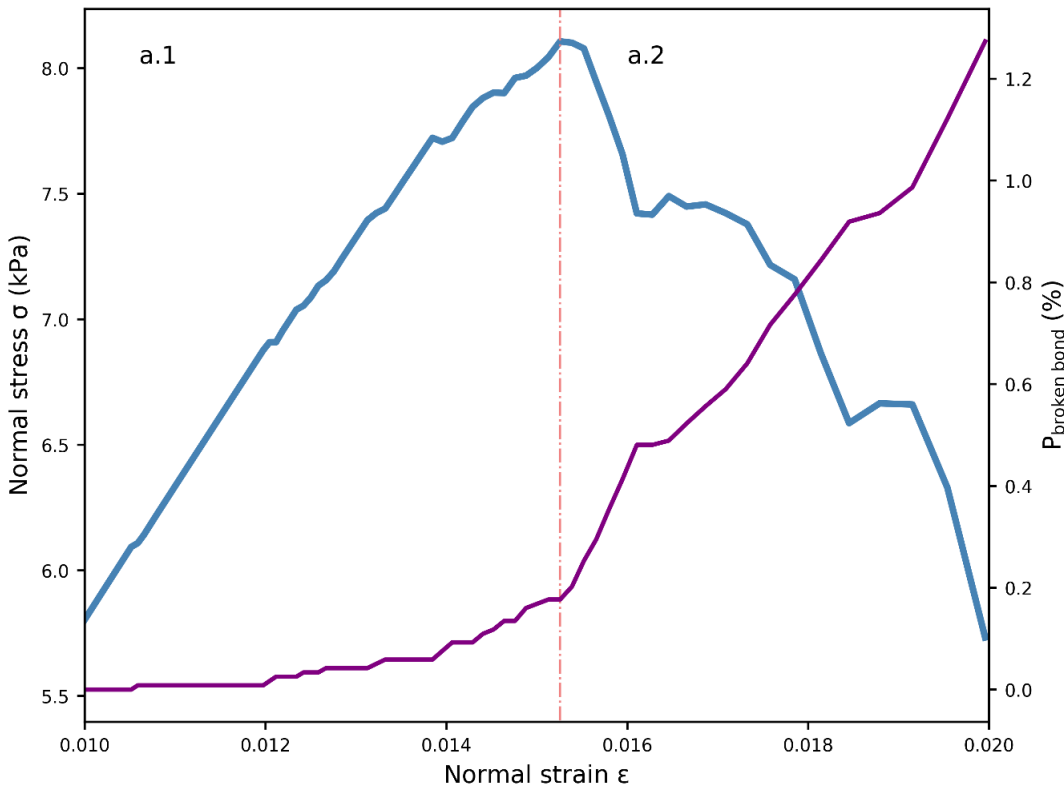
In our simulations, the fracture energy is related to the area below the stress/strain curve in the softening region. This is a result and not an input of the simulation. This fracture energy depends on the weak layer microstructure, the elastic modulus and the strength. We analyzed the results with regard to the softening ratio instead of the fracture energy which shows that the maximum acceleration and the percentage of broken bond at the end of the softening phase is driven by the softening ratio. To
 10 answer your question more specifically, the fracture energy is included in our model but we preferred to analyze our results in terms of strength of materials rather than in terms of fracture mechanics. Gaume et al. (2014) showed that the two approaches can be related to each other.

12 *In granular materials, failure mechanisms presuppose the formation and the subsequent destruction of force chains. Evidence of such behavior has been observed on real snow tests (De Biagi et al., European J. of Mech. - A/Solids, 74, 26-33, 2019). The observation of such mechanisms in simplified numerical models support the conclusions. Have the authors noted such behaviors in their tests?*

5 For computational reasons, the weak layer was modeled with around 10 vertical particles, which did not allow us to observe a clear strain localization within the weak layer. However, given for the large amount of softening we observe after failure, we expect that higher weak layer resolution would allow to observe this feature.

The figure below shows the stress–strain curve shortly before and after the peak stress; some non-linear behavior appears before failure (figure g: a.1). Following the bond-breaking position before failure (figure h) confirms the presence of initial crack formation.

10 Our simplified model does not explicitly show crack growing by clustering; this behavior could be investigated for by increasing the number of particles in the weak layer, which will increase the vertical resolution.



15 **Figure g:** Zoom of the weak layer behavior under load-controlled compression around sample failure ($E_{particle} = 30MPa$ and $\sigma_{bond}^{th} = 500kPa$). The blue line shows the normal stress before (a.1) and after (a.2) failure of the weak layer. The violet line corresponds to the proportion of broken bonds (%).

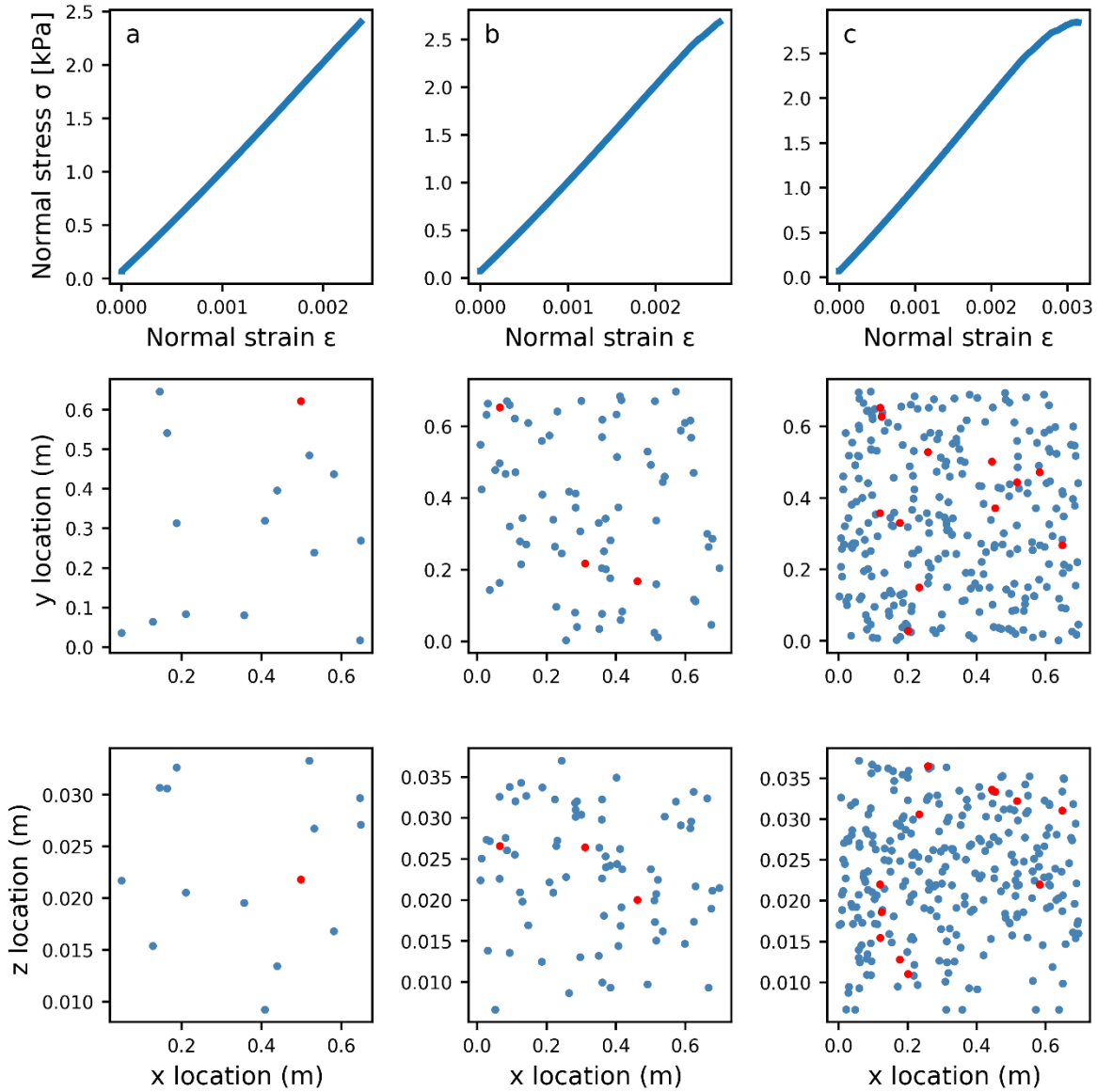


Figure h: Pre-failure crack formation. Plots (top to bottom) represent stress–strain curves, top views of the position of broken/breaking bonds in the weak layer and a side view of the position of broken/breaking bonds. Red dots represent breaking bonds and blue dots broken bonds. a. weak layer behavior at the time where the stress-strain non-linearity start (shortly before failure). b. weak layer behavior during stress-strain non-linearity. c. weak layer behavior immediately before the failure. Bonds break in spatially random manner (no localization observed)

5

References

Gaume, J., Schweizer, J., van Herwijnen, A., Chambon, G., Reuter, B., Eckert, N., and Naaim, M.: Evaluation of slope stability with respect to snowpack spatial variability, *J. Geophys. Res.*, 119, 1783-1799, <https://doi.org/10.1002/2014JF00319>, 2014.

5 Shapiro, L. H., Johnson, J. B., Sturm, M., and Blaisdell, G. L.: Snow mechanics - Review of the state of knowledge and applications, US Army Cold Regions Research and Engineering Laboratory, Hanover, N.H., U.S.A. CRREL Report 97-3, 43, 1997.

Sigrist, C.: Measurement of fracture mechanical properties of snow and application to dry snow slab avalanche release, Department of Mechanical and Process Engineering, ETH Zurich, Zurich, Switzerland, 139 pp., 2006.

10 **Reply to Referee #2**

We thank the reviewer for the insightful and constructive comments. In the following, we reply point by point on the reviewer's comments. They are shown in italic, our replies are in plain red and manuscript modification that we will make are in blue.

15 *This manuscript describes a Discrete Element Model (DEM) study of snow deformation and failure. A commercial DEM software package is used to simulate porous and anisotropic weak layers as well as denser and stronger slab layers. The size and properties of the discrete numerical particles was chosen to represent macroscopic layer properties rather than the size and shape of individual snow grains. Load-controlled numerical simulations were performed on both types of layers, using different loading orientations. The nominal stress-strain response of the simulations is discussed, and a weak layer failure*
20 *envelope is derived. Comparison is made to the results of three experiments from a cold laboratory study, with generally good agreement between the slope of the stress-strain curves and the failure stress.*

I am encouraged by the prospects for using DEM simulations to study aspects of snow mechanics and slab avalanche triggering, and this work is a welcome contribution. Most of my comments relate to issues of clarity and presentation. There is a lot of detail in the manuscript, but I find some aspects that are unclear or unsubstantiated.

25 **Thank you very much for this positive appreciation of our work. Concerning the clarity of the paper, we substantially modified our manuscript to take that comment into account. Please refer to the detailed replies below.**

Snow is a highly rate-dependent material, although the DEM model does not take into account rate effects such as sintering or viscous deformation. This is acceptable, although I think some further discussion of rate effects is warranted to place the results in context. A target "high" loading rate of 20 kPa/s is chosen for the simulations, and there is mention that verification
30 *was made that varying the loading rate did not affect the results (although this is not shown; why/how then was 20 kPa/s chosen?). However, for placing the simulation results in context with experimental results in the literature, it would be worth discussing what types of experimental loading rates are appropriate for comparing with these simulation results.*

The simulations are performed with the layer of interest (slab or weak layer) sitting on a rigid base. However, weak layers typically are sandwiched between deformable layers (slab and base are usually stiffer, but still deformable). The stress measurements from the simulations are derived from results at the interface between the layer and the rigid base. How might your results differ if you had a multi-layer scheme with a weak layer sitting on a stiffer, but deformable foundation? It seems to me that this would be more appropriate physically.

Concerning the general comment above, we discussed the hypothesis of analyzing a single layer based on the results of the concentration of deformation in the weak layer as e.g. was shown by Capelli et al. (2018) in more detail in the manuscript. Below, we reply to the specific points raised.

13 P2, L1: describe in a bit more detail what the PST is here, for the benefit of readers that may not be familiar.

10 As suggested, we added a short description in the manuscript (P.1, L.30):

Our understanding of crack propagation was greatly improved by the introduction of the Propagation Saw Test (PST; Gauthier and Jamieson, 2006; Sigrist and Schweizer, 2007; van Herwijnen and Jamieson, 2005). The PST involves isolating a snow column and initiating a crack by cutting in a pre-defined weak layer until the critical crack length is reached and self-propagation starts. The PST allows analyzing the onset and dynamics of crack propagation and deriving important mechanical properties using particle tracking velocimetry (e.g., van Herwijnen et al., 2016).

14 P2, L18-21: “too high” computational cost is vague here, and I’m skeptical of this statement without further justification. High Performance Computing (HPC) systems allow very large and costly simulations of things like climate, weather, ice sheet dynamics, astrophysics, etc. I’m quite sure that a slope-scale simulation would be feasible on a suitable HPC computing cluster, so you might just need to say that such a simulation is too costly for a stand-alone personal computer (if indeed this is what you mean), or that the commercial code you’re using isn’t suited (or licensed) for running on a large cluster.

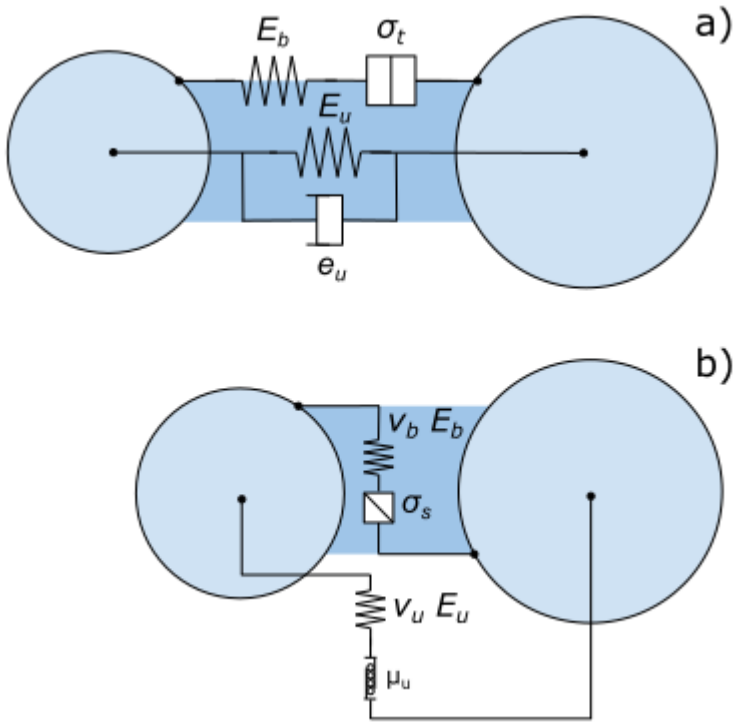
25 Simulating a load-controlled compression test for a weak layer sample of 30 cm x 30 cm requires 19,000 DEM particles. The computational costs of such a simulation on a standard personal computer (intel i7 8 processors 3.4Ghz, RAM 16Go) is 1-2 h depending on the mechanical parameters. Using a more powerful system (intel xeon 28 processors 2.6Ghz, RAM: 256Go) reduces this time to 20-30 min. The total simulation time includes two parts: about 70% of the simulation time is used to solve

the DEM equation where the time step is determined as function of the particles-contacts properties according to: $\Delta t \approx r \sqrt{\frac{\rho}{E}}$,

where $E = 40 - 480 \text{ MPa}$; this means that the DEM time step is between 10^{-6} to 10^{-8} s. The remaining about 30% of the simulation time is required to loop on contacts or particles to extract mechanical results: this looping is not parallelized on PFC software.

15 P3, L1-9: The description of the contact model is a bit vague here. A schematic diagram would be helpful to visualize what the model is simulating at the particle scale and what all these mechanical parameters represent physically. It's okay to direct the reader to previous studies that describe such an approach, to a limit, but there's just not enough information here to adequately understand the contact model.

5 We agree and described the contact model in more detail and added the following two figures in the revised manuscript (P.3, L.12).



10 **Figure i: Representation of the PFC parallel bond model (PBM) used in the simulations. a) Normal mechanical parameter bond and unbonded, where E_b represents the bond elastic modulus, σ_t the tensile strength, E_u the contact elastic modulus and e_u the restitution coefficient. b) Shear mechanical parameter bond and unbonded, where E_b represents the bond elastic modulus, σ_s the shear strength, E_u the contact elastic modulus, ν_b the bond Poisson's ratio and μ_u the friction coefficient.**

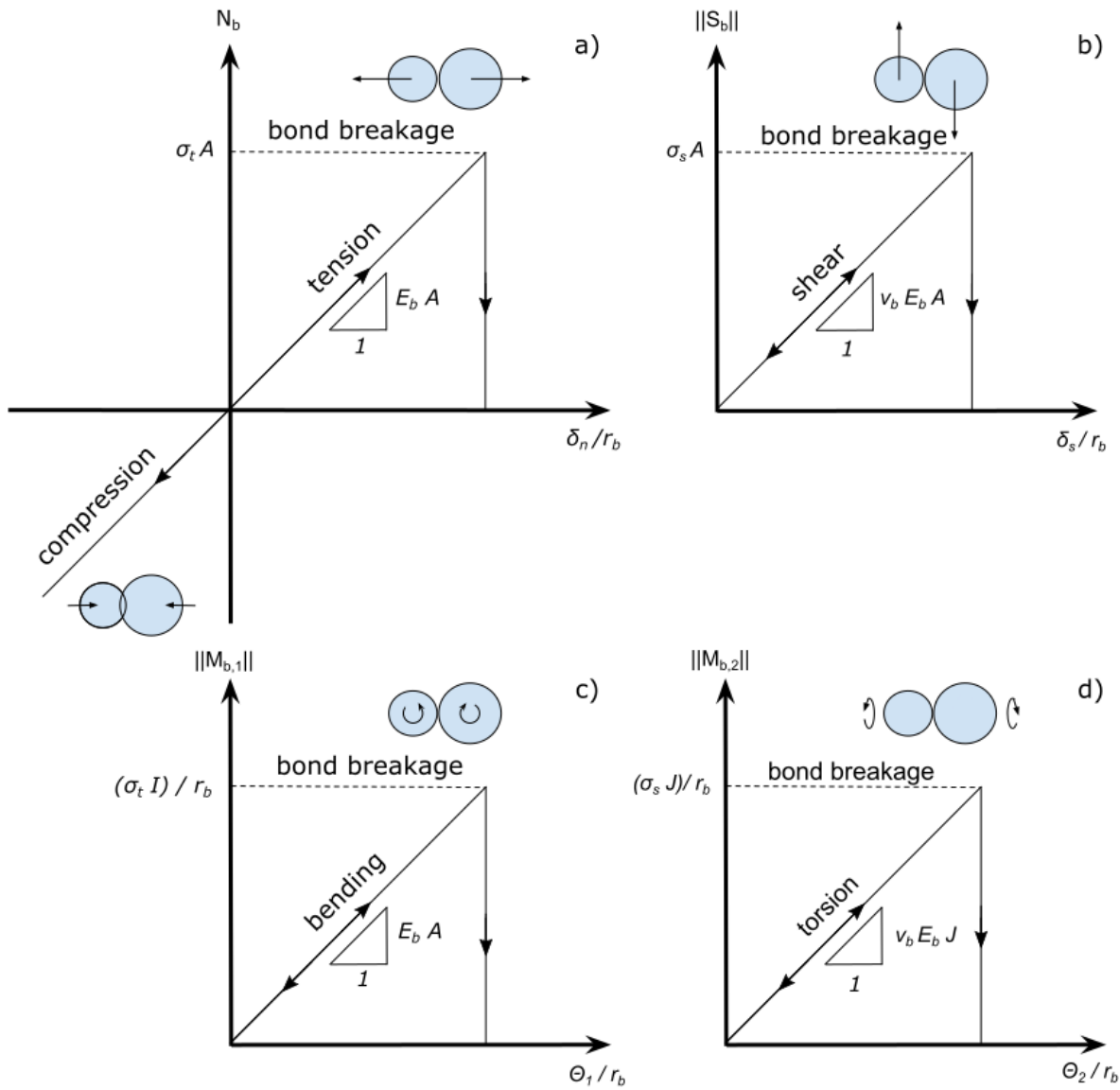


Figure j: Representation of the bonded behavior of PBM used in the simulations. (a) Bond normal force N_b as a function of the normal interpenetration δ_n scaled by the bond radius r_b . (b) Bond shear force $\|S_b\|$ as a function of tangential interpenetration δ_s scaled by the bond radius r_b . (c) Bond-bending moment $\|M_{b,1}\|$ as a function of bending rotation θ_1 scaled by the bond radius r_b . (d) Torsion moment $\|M_{b,2}\|$ as a function of twist rotation θ_2 scaled by the bond radius r_b .

16 P3 L14: “highly anisotropic” is vague: what is meant by “highly”? I might suggest removing this and just saying “anisotropic”

We removed ‘highly’ in the revised manuscript (P.3, L.22).

17 P3 L15: “can be modified by homothetic transformation” is vague here. Homothetic transformation should be defined. Is this something that is done in the present study, or just something that “can be” done?

By applying a scaling factor on the particle position and particle radius the system can be scaled up or down. The bond strength and elastic modulus are scaled such that the macroscopic mechanical behavior becomes almost exactly the same for different values of weak layer thickness (see figures c,d). A scaling factor needs to be applied to predict the failure envelope and the microscopic-macroscopic relation. The equation to characterize macroscopic properties can be written as:

$$E_{wl\ macro} = (\beta_0 + \beta_1 E_{particle}) / \left(\frac{h_{wl\ ref}}{h_{wl}}\right)$$

$$\sigma_{wl\ macro}^{th} = (\gamma_0 + \gamma_1 \sigma_{bond}^{th}) / \left(\frac{h_{wl\ ref}}{h_{wl}}\right)$$

Where $h_{wl\ ref} = 3\text{ cm}$ and h_{wl} corresponds to the new weak layer thickness.

10 This is clarified in a section that added to the supplementary material (P.3, L.24).

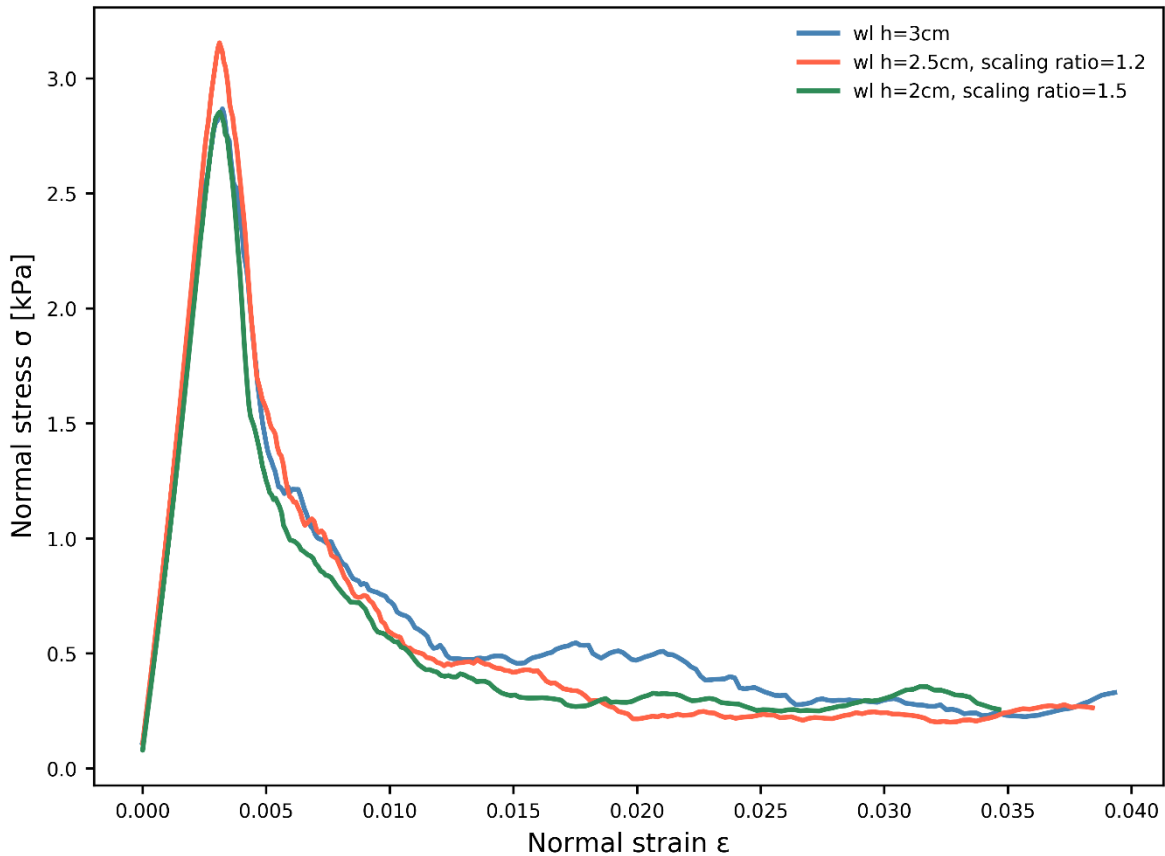


Figure k: Stress-strain curves for weak layers of different thickness (colors) under load-controlled compression. The blue line shows the reference weak layer with a thickness of 3 cm.

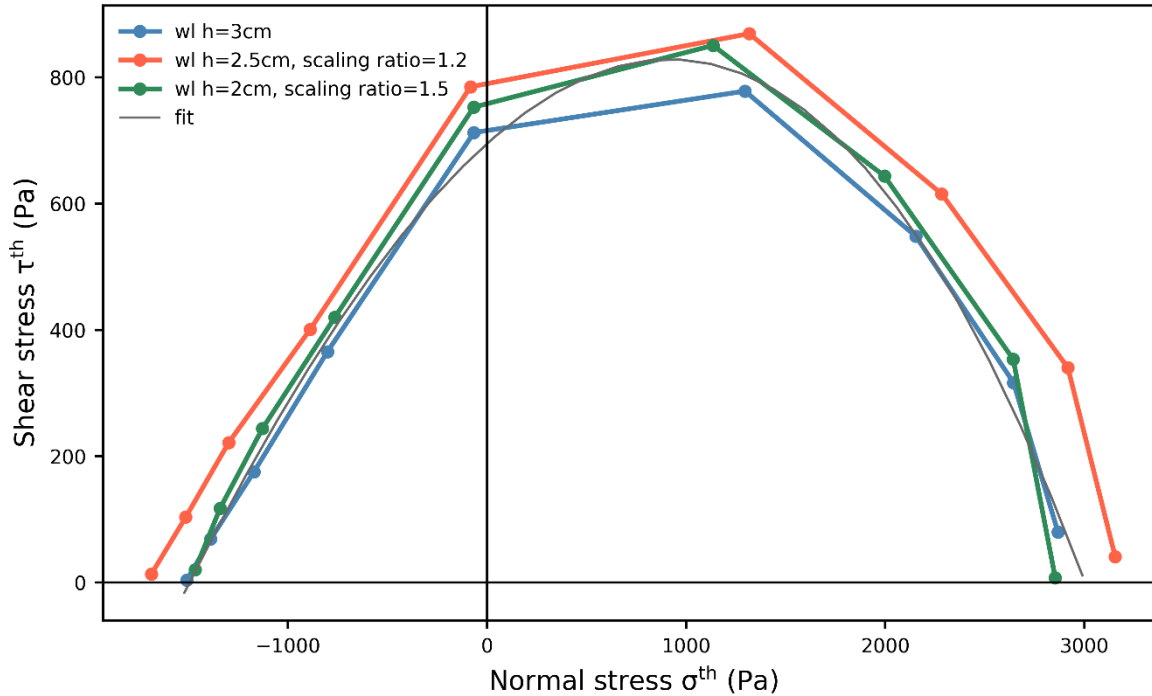


Figure l: Failure envelopes for weak layers with different thickness (colors) and fit based on equation (9).

5 18 P3 L19-20: I missed what the layer densities were that you simulated, and what particle densities were needed to achieve these layer densities. I suggest an additional table of mechanical properties such as this.

As suggested, we added the following table showing the layer properties used in the simulations (P.4,L.25).

Mechanical property	Macroscopic	Particles
Weak layer density (kg m^{-3})	110	550
Slab layer density (kg m^{-3})	250	455
Slab porosity	45%	-
Weak layer porosity	80%	-

Slab elastic modulus	0.7 – 5.5 MPa	1 – 10.5 MPa
Weak layer elastic modulus	0.5 – 7 MPa	40 – 480 MPa
Slab strength	5 – 18 kPa	6 – 19 kPa
Weak layer strength	1 – 9 kPa	70 – 560 kPa

19 **P3 L21:** *“acceptable computation time” doesn’t mean much here without a description of what kind of computer you used (later in the text you mention something about a “standard” personal computer, but this is still too vague).*

Please refer to the reply on comment #2 above.

5 **20 P3 L29:** *define “clump theory” and “clump density”*

A clump is a rigid body made of particles and follows rigid body motion (no deformation). The clump theory is defined in the manuscript as follows (P.4, L.8):

A clump is a rigid collection of n rigid particles that form one DEM element. The volume is defined by the particle positions and radius. The mass properties are defined by the clump density and clump volume. Clumps can translate and rotate but cannot deform. Clump motion obeys the equations of motion induced by the definition of mass properties, loading conditions and velocity conditions.

10

21 **P4 L1:** *it would be worth justifying why you chose unconfined test conditions rather than confined.*

Unconfined conditions were chosen to compare the results to laboratory experiments. We clarified this in the manuscript (P.4, L.3). We checked that unconfined and confined loading conditions yield the same results for weak layer behavior. This finding is due to the large porosity (80%) of the weak layer (see figure e). We added this Figure to the supplementary material.

15

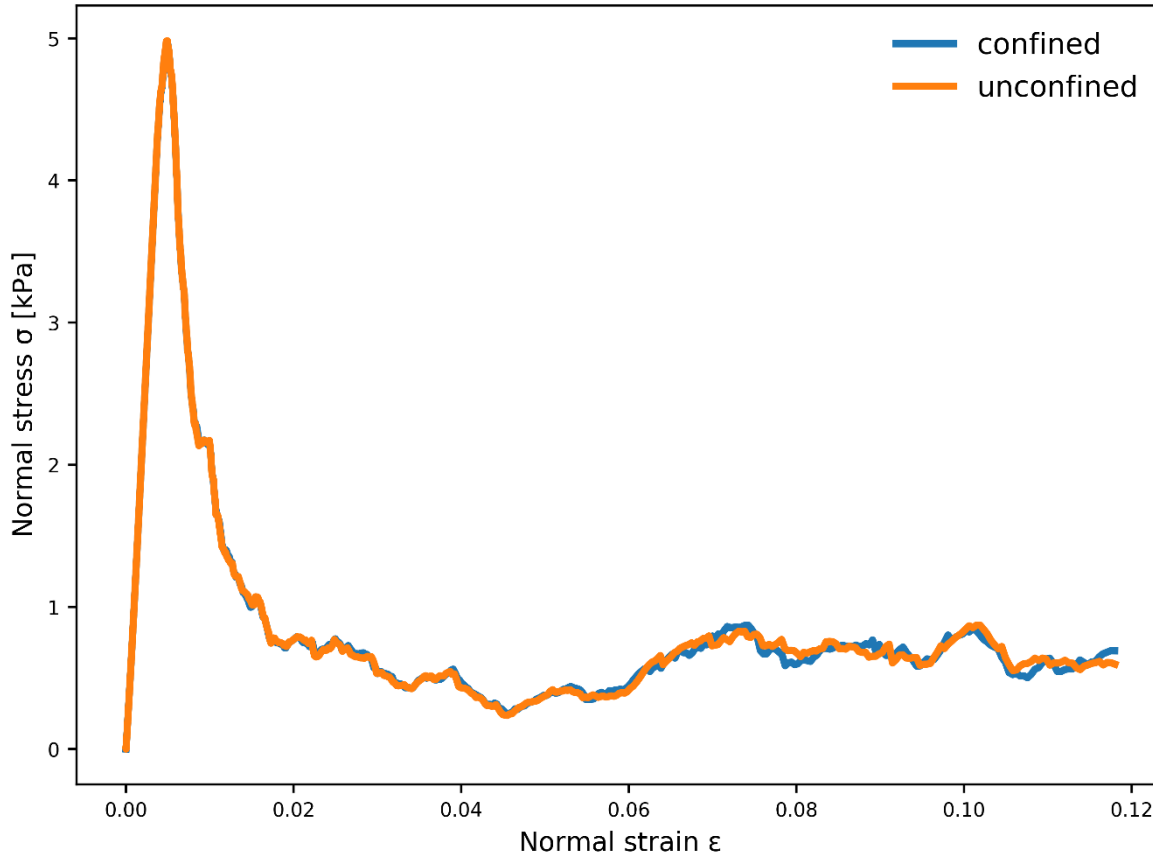


Figure m: Weak layer behavior under load-controlled compression test ($E_{particle} = 1 MPa$ and $\sigma_{bond}^{th} = 5 kPa$). The blue line shows the normal stress during confined test and the orange line during unconfined test conditions.

22 *P4 L7: I'm not clear how load-controlled tests were performed by "increasing the actuator layer density." I guess by increasing the density you're increasing the weight/gravitational acceleration that the actuator is applying to the layer? A bit more detail is needed here.*

Thank you for your comment; your guess is correct. We clarified the loading procedure in the manuscript (P.4, L.20). By increasing the density of the actuator layer (clump density), the stress is increasing.

23 *P4 L9-10: Related to comment above, here you specify a loading rate. Is this a target loading rate that you achieve by increasing the actuator density?*

We compute the simulation loading rate as the normal load ($\rho g d \cos \psi$) divided by the time step. The model is not affected by the loading rate. A loading rate of $20 kPa s^{-1}$ was chosen to reduce the computational time.

24 *P4 L19-20: Is “A” the nominal/total area or some measure of the contact area between the particles that represent the layer and the particles that represent the base?*

The area “A” is the total area of the base, this is clarified in the manuscript (P.5, L.6).

5 25 *P4 L22-23: At what point along the stress-strain curve is this tangent modulus calculated? This is a common problem with using a tangent modulus to calculate the elastic modulus, because the stress-strain curve is not usually linear all the way to the peak stress. You mention several times that these curves are linear, but I’m skeptical that this is the case. The stress-strain curves in Figures 4, 5, 6, 7, and 10 seem to show some nonlinearity right before the peak (which is to be expected, and is commonly found in experimental data; I recommend zooming in on these peaks in the figures to show any nonlinearity and bond breakage, even if minimal). Thus it really matters where you calculate a tangent modulus, and it is thus common to use something like a secant modulus at the elastic limit (something like 95% of the peak stress) for determining a more robust elastic modulus. Equation 2: I think the comma between the “i” and “j” subscripts shouldn’t be there in C_{ij} . A comma typically signifies differentiation in standard summation convention (e.g. $C_{i,j} = d/dj C_i$), but this is a tensor product of unit normal vectors.*

10 To not account for the non-linear behavior shortly before failure, we derive the elastic modulus as the secant modulus up to
15 70% of the peak stress.

Thanks for your comment, the comma should not be there and is deleted in the manuscript.

20 26 *P5 Laboratory experiments: here you chose three experiments from the Capelli study. The Capellis study looked at rate effects, and used three different loading rates. You have chosen results from their intermediate loading rate. Why? How would your results compare to their experimental results at different loading rates? Contact tensors: I’d like to see what the slab and weak layers look like in detail. It’s encouraging to see that the weak layer shows transverse isotropy. I think a figure showing the slab and weak layer assemblies in detail would be a nice addition, perhaps even with some unit normal vectors drawn in to show how you’re getting these contact tensor results.*

25 Indeed, the experiments by Capelli were done for higher loading rates (400Pa s^{-1}). The following Figure shows the direct comparison to these experiments. A loading rate of 400 Pa s^{-1} causes the shear apparatus to vibrate so that the raw data become noisy. Nevertheless, the qualitative agreement is fairly good.

We choose to analyze the behavior of each layer independently, since Capelli et al. (2018) showed that the deformation was concentrated in the weak layer. We will look into the slab and weak layer assemblies in more detail in our next study on the propagation saw test.

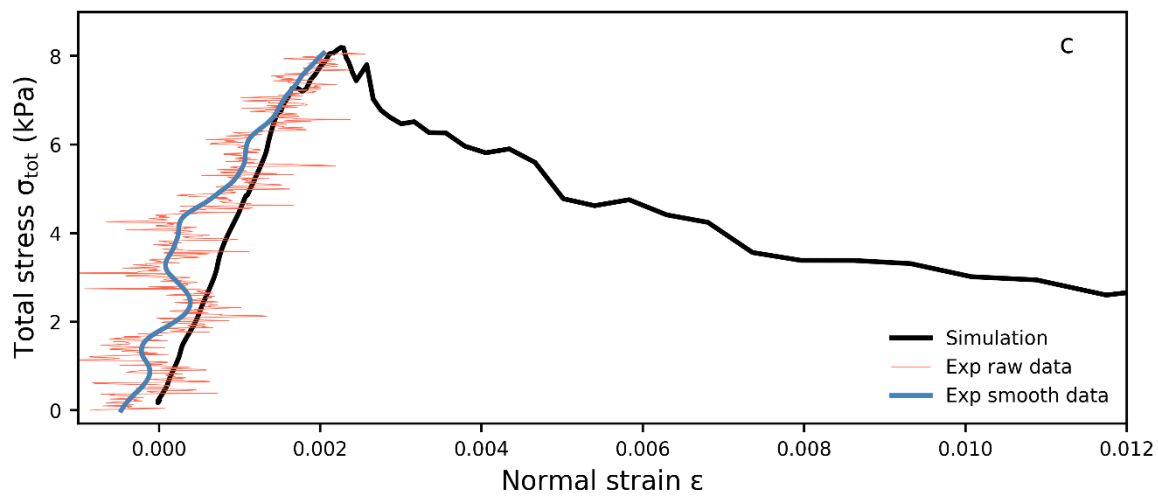
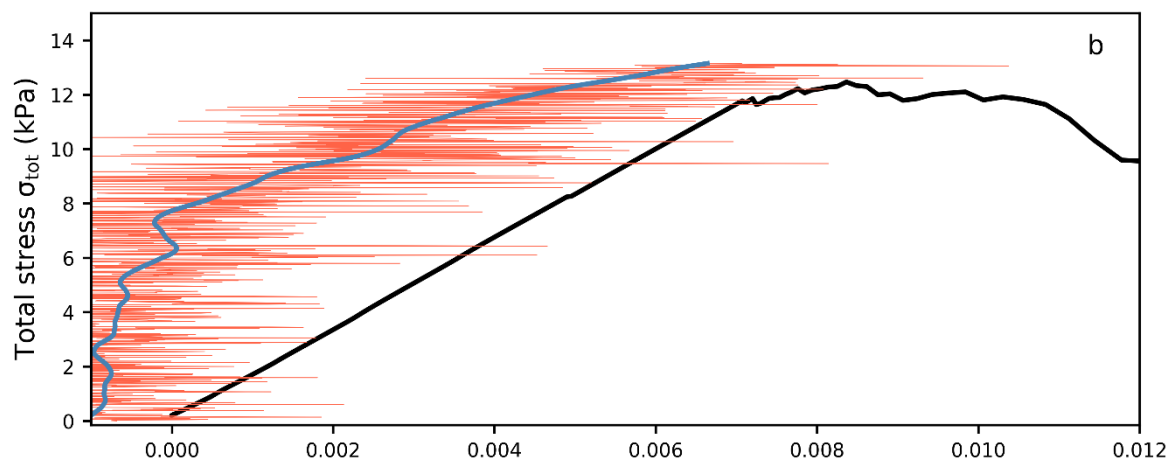
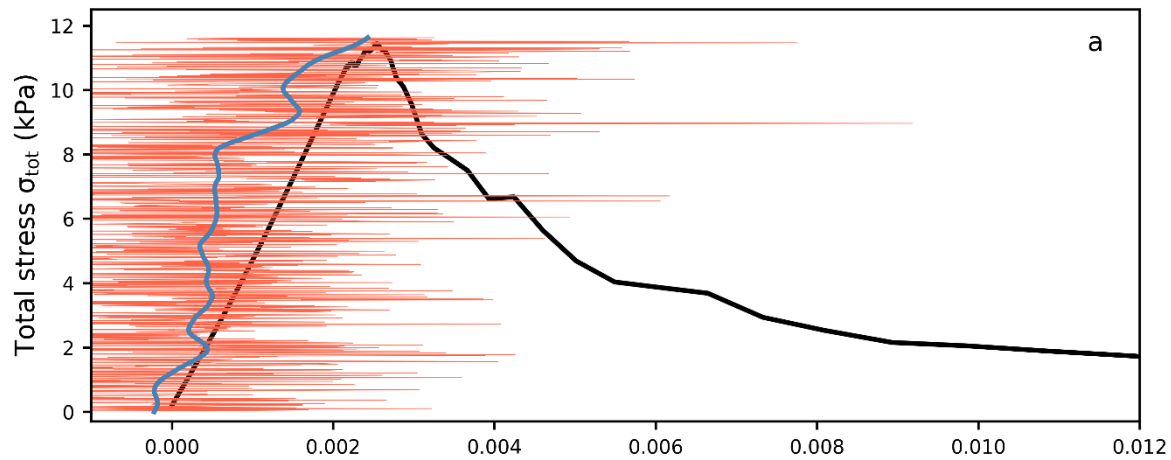
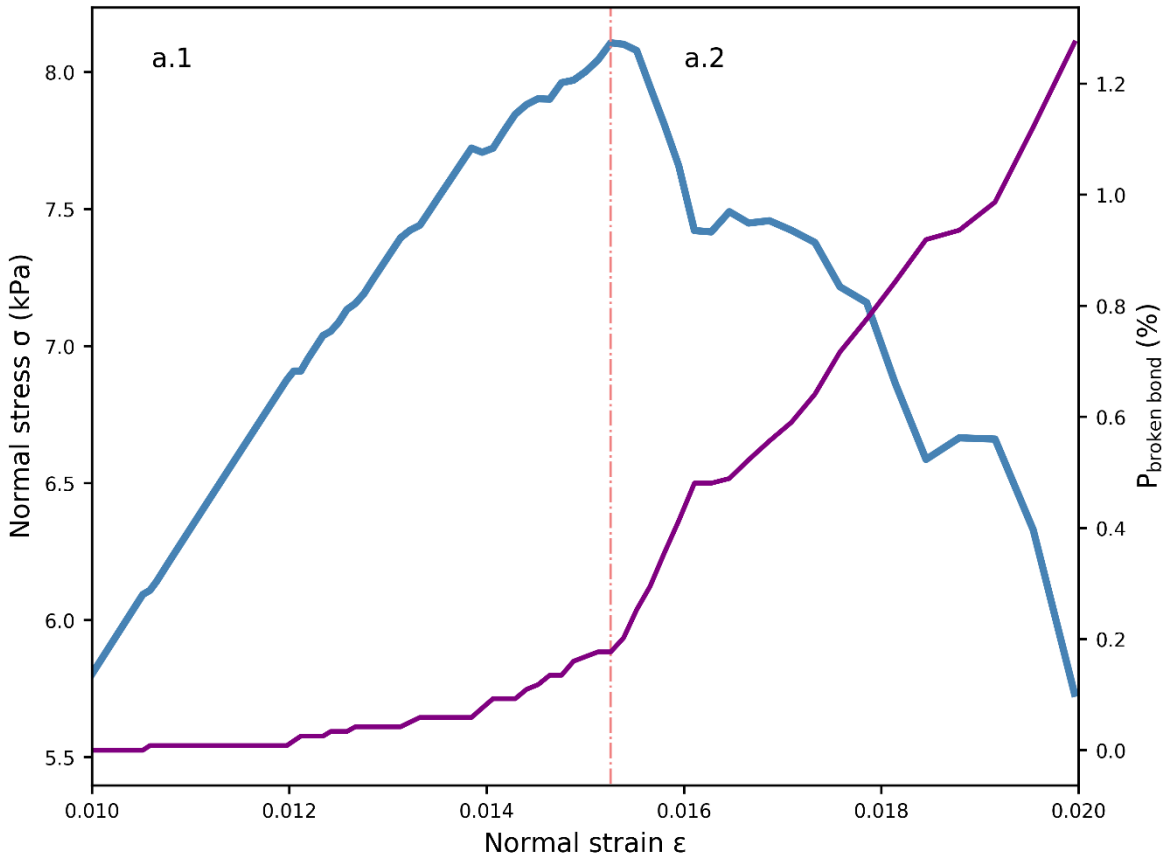


Figure n: Total stress as function of normal strain for three simulations and the corresponding experimental results done by Capelli following the procedure describe by Capelli et al. (2018) at loading rate = 400Pa/s

27 P7 L8-9: I think there is some (slight) nonlinearity right before peak, and the step in bond breaking ratio confirms this. Even a small amount of nonlinearity is important, as it indicates some damage accumulation prior to failure (and this is again why it's important where you calculate the tangent modulus...).

As you assume, there is some non-linear behavior shortly before the stress peak. The figure below shows the stress–strain curve shortly before and after peak stress (failure); we added and discussed this figure in the manuscript (P.7, L.24).



10 Figure o : Zoom of the weak layer behavior under load-controlled compression around sample failure ($E_{particle} = 30MPa$ and $\sigma_{bond}^{th} = 500kPa$). The blue line shows the normal stress before (a.1) and after (a.2) failure of the weak layer. The violet line corresponds to the proportion of broken bonds (%).

28 P7 L24: What is “Acc” and “Bond_breaking”? This seems to be new terminology. I’m also confused as to why you have focused so much on acceleration here. What exactly is the acceleration showing? You previously discuss that

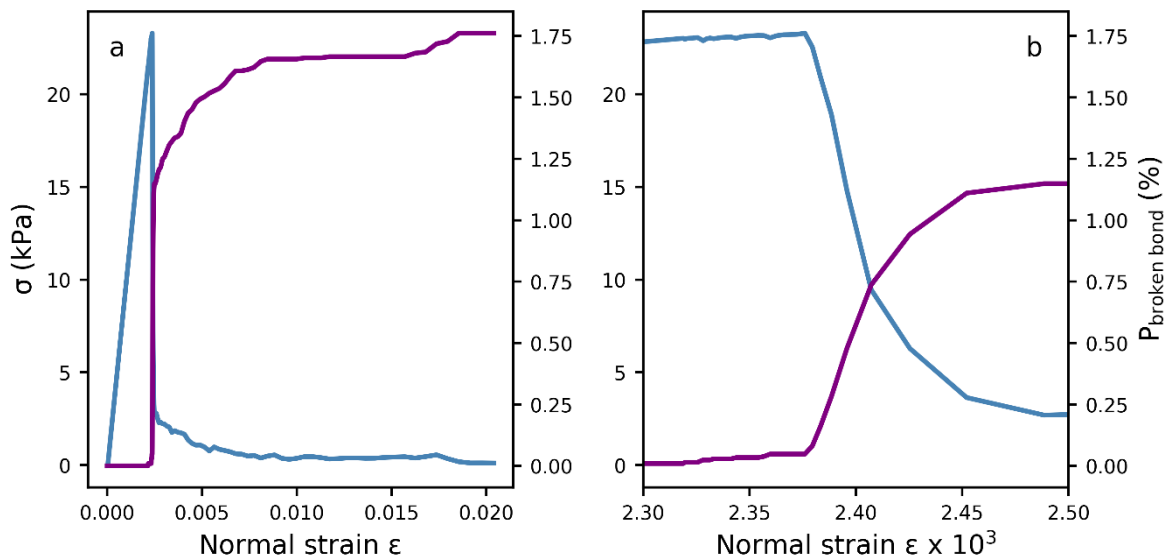
your results are not sensitive to loading rate variation, but wouldn't you expect some change in these acceleration curves with different loading rates? Even if the stress-strain curves don't change much?

Thanks for noting this mistake. "Acc" corresponds to acceleration and "Bond_breaking" to the percentage of broken bonds ($P_{broken\ bonds}$).

5 We choose to focus on the acceleration because the acceleration steeply increases at failure. We assume that this information will be useful to define the crack tip location during the crack propagation process. The differences with regard to the acceleration plateau are related to the softening ratio, which may be an important indicator for the dynamics of crack propagation.

10 29 P8 L5-6: *What do you mean by "critical" bond breaking here? The bond breaking curve in Figure 7b is obstructed by the normal strain curve, but I'm again inclined to think that there seems to be some nonlinearity/bond breaking right before failure. I would zoom in on the peaks of the stress/strain curves, perhaps in a subset of these figures.*

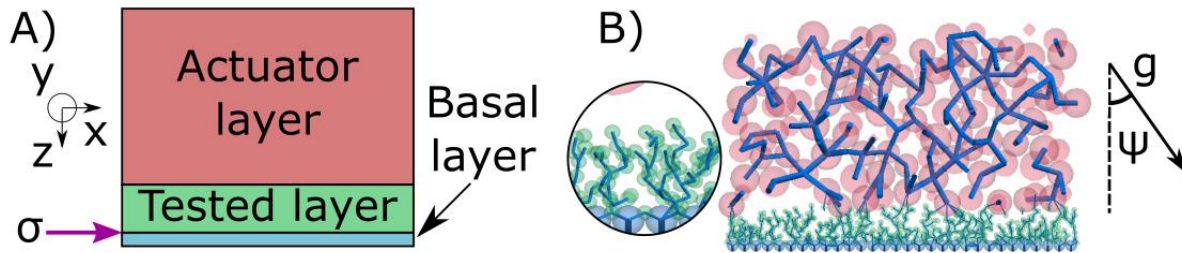
The critical bond-breaking defines the large increase of breaking bonds corresponding to catastrophic damage. A figure showing the non-linearity is added in the manuscript (P.7, L.24).



15 Figure p: a. Slab layer behavior under load-controlled tension. The blue line shows the normal stress, the violet line corresponds to the bond breaking ratio are shown as functions of the normal strain. b. Zoom around the stress peak.

30 **P8 L13:** unclear how you're defining "loading angles" here. Another example of where some schematic diagrams would be helpful.

Thanks for your comment. We improved Figure 1 in the manuscript to more clearly illustrate the test setup (P.3, L.19).



5 **Figure q:** A) Coordinate system and diagram of the setup consisting of the basal layer (blue), the tested layer, in this case a weak layer, (green) and the actuator layer (red). The violet arrow points to the interface between basal and tested layer where the stress is measured. B) slice of a generated system consisting of a slab layer (large red particles) and a porous weak layer (small green particles). A zoom of the weak layer is shown in the circle. The lines represent bonds between particles. Applied gravity is defined on the right where ψ is the loading angle.

10 31 **P8 L19:** The polynomial fit represented by Eq. 9 indeed looks good, but a goodness-of-fit measure like R^2 is not (in general) applicable for a nonlinear model unless a constant mean function can be embedded in the nonlinear model. It's worth checking how the R^2 value is calculated here, since it's not going to be the same definition for a goodness-of-fit as in a linear regression model.

Thanks for your remark, the polynomial fit coefficients was computed using least squares method which allows to compute

15 the coefficient of determination R^2 as: $R^2 = 1 - \frac{SSR}{SST}$ where SSR correspond to the residual sum of squares and SST to the total sum of squares (proportional to the variance of the data).

32 **P9 L3:** another reference to loading angles here, but the coordinate system for defining the angle hasn't been defined (some additional schematic diagrams will alleviate many of these kinds of comments) **P9 L10:** "standard personal computer" should be defined more specifically: what kind of processor, how many cores, what type/amount of memory

20 These definitions and clarifications is added in the manuscript (P.2, L.21). Please see the replies to the comments #2 and #17 above.

33 **P9 L14:** The experiments of Sigrist were in bending (to induce tensile failure), and predominantly showed quasi-brittle behaviour with clear nonlinear stress-strain (or load-displacement) response prior to failure.

As shown above in the replies to comments #15 (weak layer) and #16 (slab), there is indeed some non-linear behavior before

25 failure. We discussed the non-linear behavior shortly prior to failure in more detail in the manuscript (P.7, L.24).

34 *P9 L21-22: I can see a better agreement with the cam clay model, but less so with the Mohr-Coulomb-Cap model proposed by Reiweger, which has a linear portion corresponding to the Mohr-Coulomb criterion which is not present in your results. Perhaps worth discussing in a bit more detail, or justifying why you think there is good agreement here?*

- 5 We agree that our yield surface is close to a modified cam clay model similar to the one shown by Gaume et al. (2018). We modified the text in the manuscript as follows (P.10, L.11):

The obtained failure envelopes were qualitatively in good agreement with the Mohr-Coulomb-Cap (MCC) model proposed by Reiweger et al. (2015) and with the ellipsoid (cam clay) model proposed by Gaume et al. (2018) and Mede et al. (2018).

10 References

- Capelli, A., Reiweger, I., and Schweizer, J.: Acoustic emissions signatures prior to snow failure, *J. Glaciol.*, 64, 543-554, <https://doi.org/10.1017/jog.2018.43>, 2018.
- Gaume, J., Gast, T., Teran, J., van Herwijnen, A., and Jiang, C.: Dynamic anticrack propagation in snow, *Nat. Commun.*, 9, 3047, <https://doi.org/10.1038/s41467-018-05181-w>, 2018.
- 15 Gauthier, D., and Jamieson, J. B.: Towards a field test for fracture propagation propensity in weak snowpack layers, *J. Glaciol.*, 52, 164-168, 2006.
- Hagenmuller, P., Theile, T. C., and Schneebeli, M.: Numerical simulation of microstructural damage and tensile strength of snow, *Geophys. Res. Lett.*, 41, 86-89, <https://doi.org/10.1002/2013gl058078>, 2014.
- 20 Mede, T., Chambon, G., Hagenmuller, P., and Nicot, F.: Snow failure modes under mixed loading, *Geophys. Res. Lett.*, 45, <https://doi.org/10.1029/2018GL080637>, 2018.
- Reiweger, I., Gaume, J., and Schweizer, J.: A new mixed-mode failure criterion for weak snowpack layers, *Geophys. Res. Lett.*, 42, 1427-1432, <https://doi.org/10.1002/2014GL062780>, 2015.
- Sigrist, C.: Measurement of fracture mechanical properties of snow and application to dry snow slab avalanche release, Department of Mechanical and Process Engineering, ETH Zurich, Zurich, Switzerland, 139 pp., 2006.
- 25 Sigrist, C., and Schweizer, J.: Critical energy release rates of weak snowpack layers determined in field experiments, *Geophys. Res. Lett.*, 34, L03502, <https://doi.org/10.1029/2006GL028576>, 2007.
- van Herwijnen, A., and Jamieson, B.: High-speed photography of fractures in weak snowpack layers, *Cold Reg. Sci. Technol.*, 43, 71-82, <https://doi.org/10.1016/j.coldregions.2005.05.005>, 2005.
- 30 van Herwijnen, A., Gaume, J., Bair, E. H., Reuter, B., Birkeland, K. W., and Schweizer, J.: Estimating the effective elastic modulus and specific fracture energy of snowpack layers from field experiments, *J. Glaciol.*, 62, 997-1007, <https://doi.org/10.1017/jog.2016.90>, 2016.

Micromechanical modeling of snow failure

Grégoire Bobillier¹, Bastian Bergfeld¹, Achille Capelli¹, Jürg Dual², Johan Gaume^{1,3}, Alec van Herwijnen¹, Jürg Schweizer¹

¹ WSL Institute for Snow and Avalanche Research SLF, Davos, Switzerland

5 ² Institute for Mechanical Systems, ETH Zurich, Switzerland

³ SLAB Snow and Avalanche Simulation Laboratory, EPFL Swiss Federal Institute of Technology, Lausanne, Switzerland

Correspondence to: Grégoire Bobillier (gregoire.bobillier@slf.ch)

Abstract. Dry-snow slab avalanches start with the formation of a local failure in a highly porous weak layer underlying a cohesive snow slab. If followed by rapid crack propagation within the weak layer and finally a tensile fracture through the slab appears, a slab avalanche releases. While the basic concepts of avalanche release are relatively well understood, performing fracture experiments in the laboratory or in the field can be difficult due to the fragile nature of weak snow layers. Numerical simulations are a valuable tool for the study of micromechanical processes that lead to failure in snow. We used a three dimensional discrete element method (3D-DEM) to simulate and analyze failure processes in snow. Cohesive and cohesionless ballistic deposition allowed us to reproduce porous weak layers and dense cohesive snow slabs, respectively. To analyse the micromechanical behaviour at the scale of the snowpack (~1 m), the particle size was chosen as a compromise between low computational costs and detailed representation of important micromechanical processes. The 3D-DEM snow model allowed reproducing the macroscopic behaviour observed during compression and mixed-modes loading of dry snow slab and weak snow layer. To be able to reproduce the range of snow behaviour (elastic modulus, strength), relations between DEM particle/contact parameters and macroscopic behaviour were established. Numerical load-controlled failure experiments were performed on small samples and compared to results from load-controlled laboratory tests. Overall, our results show that the discrete element method allows to realistically simulate snow failure processes. Furthermore, the presented snow model seems appropriate for comprehensively studying how the mechanical properties of slab and weak layer influence crack propagation preceding avalanche release.

25 35 Introduction

Dry-snow slab avalanches require initiation and propagation of a crack in a weak snow layer buried below cohesive slab layers. Crack propagation occurs if the initial zone of damage in the weak layer is larger than the so-called critical crack size. Weak layer fracture during crack propagation is generally accompanied by the structural collapse of the weak layer due to the high porosity of snow (van Herwijnen et al., 2010). If the crack propagates across a steep slope, a slab avalanche may release (McClung, 1979; Schweizer et al., 2003). **Our understanding of crack propagation was greatly improved by the introduction of the Propagation Saw Test (PST; Gauthier and Jamieson, 2006; Sigrist and Schweizer, 2007; van Herwijnen and Jamieson,**

2005). The PST involves isolating a snow column and initiating a crack by a sawing in a pre-defined weak layer until the critical crack length is reached and self-propagation starts. The PST allows analysing the onset and dynamics of crack propagation and deriving important mechanical properties using particle tracking velocimetry (van Herwijnen et al., 2016). The essential mechanical properties related to the onset of crack propagation are slab elasticity, slab load and tensile strength, as well as the weak layer strength and specific fracture energy (e.g., Reuter and Schweizer, 2018). However, no theoretical framework exists that describes how these mechanical properties and possibly other ones such as the weak layer failure envelope, weak layer elasticity or microstructure relate to the dynamics of crack propagation at the slope scale. Whereas field experiments are difficult to perform at this scale, numerical simulations may provide insight into the drivers of propagation dynamics.

Johnson and Hopkins (2005) were the first to apply the discrete element method (DEM) to model snow deformation. They simulated creep settlement of snow samples, which consisted of a 1000 randomly oriented cylinders of random length with hemispherical ends. More recently, DEM was used to model the mechanical behaviour based on the complete 3-D microstructure of snow (Hagenmuller et al., 2015). Gaume et al. (2015) developed a discrete element model to simulate crack propagation and subsequently derived a new analytical expression for the critical crack length (Gaume et al., 2017b). Their approach allows generating highly porous samples and was used to perform 2-D simulations of the PST in agreement with field experiments. However, the oversimplified shape (triangular structure) and the 2-D character of the weak layer employed by Gaume et al. (2015) prevented a detailed analysis of the internal stresses during crack propagation. On the other hand, microstructure-based DEM models adequately reproduce the mechanical behaviour (Mede et al., 2018). However, the computational costs of these complex 3D-models are too high to generate samples large enough to investigate the dynamics of crack propagation at the slope scale on a standard personal computer (Intel i7 8 processors 3.4 GHz, RAM 16Go).

Our aim is to develop a 3-D DEM snow model that adequately takes into account snow microstructure, but is not too costly in terms of computational power so that simulations at the slope scale become feasible on a High Performance Computer (HPC). To relate DEM parameters to macroscopic snow behaviour we will validate the model by simulating basic load cases. Finally, we numerically simulate mixed-mode loading experiments and compare results to those obtained during laboratory experiments.

36 Data and methods

36.1 Formulation of the model

Discrete element method

To simulate the failure behaviour of layered snow samples, we used the discrete element method (DEM). DEM, first introduced by Cundall and Strack (1979) is a numerical tool, commonly employed to study granular-like assemblies composed of a large

number of discrete interacting particles. We used the PFC3D (v5) software developed by Itasca Consulting Group (<http://www.itascacg.com>).

Contact model

We used the parallel-bond contact model (PBM) introduced by Potyondy and Cundall (2004). PBM provides the mechanical behavior of a finite-sized piece of cement-like material that connects two particles. The PBM component acts in parallel with a classical linear contact model and establishes an elastic interaction between the particles. The mechanical parameters include the contact elastic modulus E_u , Poisson's ratio $\nu_u = 0.3$, the restitution coefficient $e_u = 0.1$, and the friction coefficient $\mu_u = 0.2$. If particles are bonded, the bond part will act in parallel to the contact part. The bonded part is described by the bond elastic modulus E_b , the bond Poisson's ratio $\nu_b = 0.3$ and the bond strength, shear and tensile strength σ_s and σ_t . To reduce the number of variables we assume $E_u = E_b \triangleq E_{particle}$ and $\sigma_s = \sigma_t \triangleq \sigma_{bond}^{th}$. **Figure 18 illustrates the PFC parallel bond model (PBM) with the mechanical parameters for the bonded and unbonded state. Four different bond behaviours (tension/compression, shear, bending and torsion) are shown Figure 19. More details on the PBM can be found in previous studies (Gaume et al., 2015; Gaume et al., 2017a; Gaume et al., 2017b). Once a bond breaks, only particle frictional contact occurs and no new bonds are created (i.e. no sintering occurs). This assumption is motivated by the fact that the strain rate is large and the time scale is seconds during the post-failure phase.**

System generation

The simulated three-dimensional system consisted of a rigid basal layer (Figure 20, blue particles), the layer studied (weak layer or slab layer, green particles), and an 'actuator' layer used to apply the load (red particles). The basal layer is composed of a single layer of particles with a radius of $r = 5$ mm. The weak layer was created by cohesive ballistic deposition (Löwe et al., 2007) to reproduce the porous and anisotropic structure of natural weak layers. Doing so, we obtained a porosity of 80% for a particle radius of $r = 2.5$ mm. The layer thickness (3 cm) can be modified by homothetic transformation while keeping the same mechanical behaviour. **A short weak layer scaling study is provided in the supplementary material.**

We used cohesionless ballistic deposition to generate dense layers (Kadau and Herrmann, 2011) as typically found in snow slab layers. For these layers we used a particle radius of $r = 11 \pm 1$ mm (uniform distribution). The radius variation was introduced to prevent close packing, resulting in a porosity of 45%. Layer density (ρ) was adjusted by changing the particle density. The size of the particles is not intended to represent the real snow grains. The particle size was chosen as a trade-off between an acceptable computation time (min to day) and avoiding particle size effects in the numerical experiments. At the defined particles scale (larger than the snow grains) the ice properties (e.g. strength, elastic modulus, Poisson's ratio) cannot be used directly. Therefore, the particle scale can be considered as a mesoscale between the macroscopic scale (sample scale) and the microscale (individual snow grains). Hence, we adjusted the particle density to represent the macroscopic snow densities in accordance with the macroscopic sample porosity.

To characterize the mechanical behaviour of these two types of snow-like layers (weak layer or slab layer), **unconfined load-controlled tests were performed and compared to experimental results.** We also performed **confined compression tests, but found no difference in behaviour compared to the unconfined tests due to the porosity of 80% (shown in the supplementary material).** To simulate the tests, we added an 'actuator' layer generated by cohesionless ballistic deposition, composed of particles of radius $r = 10$ mm on top of the studied layer (Figure 20, red particles). This layer is defined as a rigid clump with initially low density. **A clump is a rigid collection of n rigid particles that form one DEM element. The volume is defined by the particle positions and radius. The mass properties are defined by the clump density and clump volume. Clumps can translate and rotate but cannot deform. Clump motion obeys the equations of motion induced by the definition of mass properties, loading conditions and velocity conditions.**

The samples were generated in a box; the box walls were then removed to create unconfined test conditions. To avoid a packing effect at the sidewalls, samples were generated 10 particle radius larger and cutout before the simulation. In order to model macroscopic mechanical behaviour of the studied layers, we tuned the particle elastic modulus and the bond strength. A large range of particle elastic modulus and bond strength were tested to characterize the relation between particle parameters and macroscopic behaviour. **In some materials, strength and elastic modulus are related, while in other materials these properties are independent. For snow, it remains unclear whether the two properties are related. Our goal was to independently control both parameters in order to have a precise control on the macroscopic elastic modulus and macroscopic strength of the snow.**

Load-controlled test

Load-controlled simulations were performed by increasing **linearly** the actuator layer density. To avoid a sample size effect (see below), 30 cm \times 30 cm samples were generated. Our DEM model does not take into account viscous effects or sintering of snow, therefore the results do not depend on the loading rate (not shown). We chose a high loading rate of 20 kPa s⁻¹ simply to reduce the simulation time but we verified that the loading rate did not affect the results. **By changing the angle of gravity (ψ in Figure 20), mixed-mode loading was simulated. Failure was defined as the point of maximum shear or normal stress during the two first phases (linear elastic and softening phases). Table 1 summarizes the particle mechanical properties used for simulations and their corresponding macroscopic values.**

25 *Time step*

The length of the time step was determined as function of the particle properties according to

$$\Delta t \approx r \sqrt{\frac{\rho}{E}} \quad (1)$$

where ρ and r are the smallest particle density and radius, respectively, and E is the largest bond or particle elastic modulus. Choosing the time step in this manner ensures the stability of the DEM model (Gaume et al., 2015).

Stress and strain

The average stress and strain were calculated at the interface between the rigid base layer and the studied layer (Figure 20, violet arrow). Normal stress $\bar{\sigma}_z$ was computed as $\bar{\sigma}_z = F_z/A$ and shear stress as $\bar{\sigma}_x = F_x/A$. Here F_x and F_z are the sum of the contact forces acting on the basal layer in the tangential and normal direction, respectively, and A is the total area of the basal layer over which the stresses were determined. We define the engineering strains as normal strain: $\varepsilon_z = \frac{u_z}{D}$ and shear strain: $\gamma_x = \frac{u_x}{D}$ with the displacement of the actuator u in the z- and x-directions and the thickness D of the studied layer. **The macroscopic strength (σ^{th}) was defined as the maximum stress before catastrophic failure.** The macroscopic elastic modulus (E) was defined on the normal stress-strain curve as the derivative of the stress between 0 and 70% of the stress peak.

Fabric tensor

10 If the particle arrangement during layer creation is not isotropic, the mechanical quantities of the layer show directional dependency. For any heterogeneous, anisotropic material (e.g. bones, concrete, snow), the fabric tensor characterizes the geometric arrangement of the porous material microstructure. The fabric tensor, referred to here as the contact tensor C , is the volume average of the tensor product of the contact unit normal vectors \bar{n} . The 2nd order contact tensor coefficients are defined in Ken-Ichi (1984) as:

$$15 \quad C_{ij} = \frac{1}{N} \sum_{\alpha=1}^N n_i^\alpha n_j^\alpha \quad (2)$$

where N is the total number of particle contacts, and n_i^α are the normalized projections of the contact with respect to the x_i Cartesian coordinate (Shertzer et al., 2011). The contact tensor C was used to estimate the physical properties of the simulated sample.

36.2 Laboratory experiments

20 For model validation, we used data of cold laboratory experiments obtained with a loading apparatus described in Capelli et al. (2018). They performed load-controlled failure experiments on artificially created, layered snow samples, consisting of a weak layer of depth hoar crystals between harder layers of fine-grained snow. The load applied on the samples was increased linearly until the sample failed. For more information on the experiments see Capelli et al. (2018). We selected three experiments (Table 2) for validating the numerical simulations. For the validation we focused on the normal strain, since for
25 the experimental shear strain data (measure of the horizontal displacement) the signal-to-noise ratio was too low. Furthermore, due to the method used to load the snow samples, data from the force sensor after failure contained experimental artefacts. To select the model parameters $E_{particle}$ and σ_{bond}^{th} , we used the elastic modulus computed as the derivative of the normal stress-strain curve and the strength values from the experiments (Table 2), as well as the relations for strength and modulus derived

below. Digital image analysis of the experiments had revealed that the deformation was concentrated in the weak layer (Capelli et al., 2018). We therefore simulated the weak layer with a rigid actuator layer on the top.

37 Results

This section first presents the structural properties of the two generated layers. The two generated layers were analysed based on an unconfined compression test. Then, the link between macroscopic behaviour and particle properties is described. Finally, the model setup for the weak layer is validated by comparing numerical mixed-modes loading simulations to experimental data.

37.1 Structural properties of generated samples

For the sample used to generate the slab, the coefficients of the contact tensor C were (Eq. 2):

$$10 \quad C_{slab} = \begin{bmatrix} 0.32 & 0 & 0 \\ 0 & 0.32 & 0 \\ 0 & 0 & 0.35 \end{bmatrix} \quad (3)$$

This shows that the slab samples are nearly isotropic, which is in line with results reported for snow types typically found in snow slab layers (Gerling et al., 2017; Srivastava et al., 2016).

For the weak layer samples, 5 in total, the contact tensor was:

$$C_{weak\ layer} = \begin{bmatrix} 0.27 & 0 & 0 \\ 0 & 0.27 & 0 \\ 0 & 0 & 0.46 \end{bmatrix} \quad (4)$$

15 It shows transverse isotropic symmetry that is again in line with data from snow samples representative for weak layers (i.e. layers of depth hoar, surface hoar or facets), which also show transverse isotropy (Gerling et al., 2017; Shertzer, 2011; Shertzer et al., 2011; Srivastava et al., 2016).

37.2 Characterization of macroscopic properties

Slab layer

20 To establish a relationship between the macroscopic elastic modulus and the particle elastic modulus, we performed 100 simulations (with ten different values of $E_{particle}$ and ten different values of σ_{bond}^{th}) in pure compression to relate macroscopic and particle parameters. The macroscopic elastic modulus increased linearly with $E_{particle}$:

$$E_{slab\ macro} = \beta_0 + \beta_1 E_{particle} \quad (5)$$

with the coefficients $\beta_0 = 1.5 \times 10^5$ Pa and $\beta_1 = 0.526$ (dashed line in Figure 21a; $R^2 = 0.981$).

The macroscopic strength also increased linearly with bond strength

$$\sigma_{slab\ macro}^{th} = \gamma_0 + \gamma_1 \sigma_{bond}^{th} \quad (6)$$

with the coefficients $\gamma_0 = -318$ Pa and $\gamma_1 = 0.982$ (dashed line in Figure 21b; $R^2 = 0.999$).

Weak layer

- 5 For the weak layer we performed 81 simulations (with nine different values of $E_{particle}$ and nine different values of σ_{bond}^{th}) in pure compression to relate macroscopic and particle parameters. The macroscopic elastic modulus increased linearly with $E_{particle}$:

$$E_{wl\ macro} = \beta_0 + \beta_1 E_{particle} \quad (7)$$

with coefficients $\beta_0 = 7.3 \times 10^4$ Pa and $\beta_1 = 0.014$ (Figure 22a; $R^2 = 0.985$).

- 10 The macroscopic strength also increased linearly with bond strength

$$\sigma_{wl\ macro}^{th} = \gamma_0 + \gamma_1 \sigma_{bond}^{th} \quad (8)$$

with coefficients $\gamma_0 = 76.7$ Pa and $\gamma_1 = 0.016$ (Figure 22b; $R^2 = 0.998$).

Hence, based on equations (7) and (8), any values of the macroscopic quantities $\sigma_{wl\ macro}^{th}$ and $E_{wl\ macro}$ can be obtained by tuning $E_{particle}$ and σ_{bond}^{th} .

15 37.3 Mechanical behaviour of layers

Slab layer

- To investigate the mechanical behaviour of the slab layer, we performed load-controlled tension tests. Two phases can be distinguished: linear elastic deformation followed by sample fracture. During the linear elastic deformation, no bond damage appears and the stress linearly increase up to $\varepsilon = 0.0025$ (Figure 23). At failure, the stress dropped rapidly and bond damage
20 drastically increased with increasing strain.

Weak layer

- The large-deformation, unconfined load-controlled compression tests of weak layer samples revealed four different phases (grey dashed-dotted lines in Figure 7). First, there was a linear elastic phase without bond breaking (a.1), non-linearity appears
25 right before the stress peak induced by some damage prior to failure; in good agreement with the quasi-brittle behaviour of weak snow layers (Figure 25). When the macroscopic strength was reached, the normal stress dropped sharply during the softening phase as bond damage increased drastically (a.2). During the brittle crushing phase, the sample density as well as

the proportion of broken bonds ($P_{broken\ bond}$) steadily increased (a.3). Finally, the densification phase (a.4) was reached when the stress prominently increased again as the particles were closely packed.

By varying the particle modulus $E_{particle}$ and the bond strength σ_{bond}^{th} the micromechanical behaviour in terms of bond breaking and acceleration (a) of the actuator layer was also investigated more closely up to the start of the brittle crushing phase (Figure 26). Before reaching the macroscopic strength, the normal stress increased linearly with increasing strain while the number of broken bonds and the acceleration were low. The strain at failure depended on both $E_{particle}$ and σ_{bond}^{th} . During the softening the stress sharply dropped while both the number of broken bonds and the acceleration increased. Both $E_{particle}$ and σ_{bond}^{th} controlled the amount of stress drop as well as the rate of increase of $P_{broken\ bond}$ and a. During the brittle crushing phase, both strength and acceleration did not change while $Bond_{breaking}$ increased, independent of the values of $E_{particle}$ and σ_{bond}^{th} .

The stress at the end of the softening phase was characterized by the softening ratio $R = \frac{\hat{\sigma}_{residual}}{\sigma_{wl\ macro}^{th}}$ with $\sigma_{wl\ macro}^{th}$ the macroscopic strength and $\hat{\sigma}_{residual}$ the mean residual stress during the brittle crushing phase. The test with the highest softening ratio (Figure 26 solid light blue line: $R = 0.45$) showed the lowest damage and the lowest acceleration. In contrast, the lowest softening ratio (Figure 26 dark blue dashed line: $R = 0.21$) corresponded to the largest proportion of broken bonds and the largest acceleration. Concerning the two other tests, they exhibited the same residual stress but different softening ratios. We observed that the softening ratio followed a non-linear relation with $E_{particle}$ and σ_{bond}^{th} .

Similar to the behaviour under compression, the mechanical response in shear exhibited different phases: an elastic phase, softening and simultaneously normal brittle crushing and shear displacement and finally shear displacement only (grey dashed-dotted lines in Figure 10). Also the damage dynamics were similar as in pure compression (Figure 10b). No critical bond breaking was observed during the linear elastic phase followed by catastrophic damage after failure. Subsequently, the damage further increased during the brittle crushing. The normal strain increased during the brittle crushing phase and did not change thereafter. The normal deformation was closely related to the proportion of broken bonds, similar to behavior in the pure compression. Shear and normal accelerations reached their maximum at the end of the softening phase (Figure 27c) as observed in pure compression (Figure 24). During the brittle crushing phase, the normal acceleration decreased due to the creation of new contacts that decelerate the actuator layer. The **tangential acceleration** did not change much during the shear displacement phase.

Weak layer failure envelope

Unconfined load-controlled tests with nine loading angles were performed to create the failure envelope. Figure 28 compiles the values of macroscopic strength for different loading angles resulting in a failure envelope including tension (negative normal stress), pure shear, pure compression as well as mixed-mode loading states. To investigate the influence of sample size,

we performed a sensitivity analysis by varying the sample size from $0.1 \text{ m} \times 0.1 \text{ m}$ to $1 \text{ m} \times 0.6 \text{ m}$ and the random deposition (generation of different ball positions for the ballistic deposition). Apart from the smallest sample, all samples had very similar failure envelopes, which were fitted with 2nd order polynomial with coefficients $\beta_0^{FE} = -7.66 \times 10^2 \text{ Pa}$, $\beta_1^{FE} = -0.25$, $\beta_2^{FE} = 1.97 \times 10^{-4}$ (dash-dotted black line in Figure 28, $R^2 = 0.97$):

$$5 \quad \tau^{th} = \beta_2^{FE} \sigma^{th^2} + \beta_1^{FE} \sigma^{th} + \beta_0^{FE} \quad (9)$$

For a sample length of 0.3 m or larger, no effect of sample size on the failure envelope was observed. The sample heterogeneity induced by different types of random deposition did not influence the failure envelope either. Given the expression for the macroscopic strength (Eq. 9) where σ^{th} represents the normal strength and τ^{th} the shear strength, the failure envelope is directly related to σ_{bond}^{th} .

10 As the macroscopic strength σ_{wl}^{th} is related to σ_{bond}^{th} (Eq. 8), the failure envelope can be scaled by using the scaling factor $\left(\frac{\sigma_{wl}^{th}}{\sigma_{wl\ ref}^{th}}\right)$:

$$\tau^{th} = (\beta_2^{FE} \sigma^{th^2} + \beta_1^{FE} \sigma^{th} + \beta_0^{FE}) \frac{\sigma_{wl}^{th}}{\sigma_{wl\ ref}^{th}}, \quad (10)$$

with $\sigma_{wl\ ref}^{th} = 2650 \text{ Pa}$, which corresponds to the maximum strength in pure compression (Figure 28). Equation (10) allows deriving the failure envelope for any value of the bond strength σ_{bond}^{th} (green dash-dotted lines in Figure 29).

15 **37.4 Comparison with experimental data**

To validate the behaviour of our simulated weak layer samples, we used data from laboratory experiments performed by Capelli et al. (2018) (Table 2). For each of the three experiments with different loading angles the simulated total stress ($\sigma_{tot} = \sqrt{\sigma^2 + \tau^2}$) as function of normal strain (ε) was in good agreement with the experimental results (Figure 30).

38 Discussion

20 We used 3-D discrete element modelling to study the mechanical behavior of simplified snow samples generated by different ballistic deposition techniques. Cohesive ballistic deposition produced transversally isotropic weak layers with high porosity (80%). Cohesionless ballistic deposition produced isotropic slab layers of lower porosity (45%), in general agreement with key properties of natural snow samples (Shertzer, 2011). The DEM particles do not represent real snow grains, to keep the computational costs reasonable (i.e. ~10 min on a standard personal computer for a sample of $50 \text{ cm} \times 50 \text{ cm}$ in size, 25 corresponding approximately to 26,500 particles). By varying the DEM particle parameters $E_{particle}$ and σ_{bond}^{th} the macroscopic properties can be modified to fit different types of snow.

First, tension tests were simulated to study the behaviour of dense slab layers. The results evidenced an almost perfectly brittle behaviour in good agreement with the tensile behaviour reported by Hagenmuller et al. (2014) and by Sigrist (2006).

The mechanical behaviour we observed for our weak layer samples, in particular the four phases (Figure 24) during a load-controlled compression test, were very similar to those reported by Mede et al. (2018) who simulated snow behaviour with microstructure-based snow samples. More generally, Gibson and Ashby (1997) also described these four distinct phases for elastic-brittle foam samples.

The unconfined load-controlled tests under mixed-mode loading conditions showed shear behaviour in good agreement with previously reported results (Mede et al., 2018; Mulak and Gaume, 2019; Reiweger et al., 2015).

The obtained failure envelopes were qualitatively in good agreement with the Mohr-Coulomb-Cap (MCC) model proposed by Reiweger et al. (2015) and with the ellipsoid (cam clay) model proposed by Gaume et al. (2018) and Mede et al. (2018). The model qualitatively reproduced the snow failure envelopes found in other numerical studies (Mede et al., 2018; Mulak and Gaume, 2019). In our case, the failure envelope is directly linked to σ_{bond}^{th} , since any failure envelope can be expressed as a function of σ_{bond}^{th} . Weak layer failure behaviour was not affected by the heterogeneity induced by different types of random ball deposition and by the sample size if the sample size was larger than $0.3 \text{ m} \times 0.3 \text{ m}$. This size is typically found in field tests (PST, ECT; Bair et al., 2014; Reuter et al., 2015; van Herwijnen et al., 2016) and laboratory experiments (Capelli et al., 2018).

Based on these purely numerical investigations, the particle and contact parameters were selected to reproduce the results of cold laboratory experiments with real snow samples (Figure 13). The numerical results were qualitatively in good agreement for the three loading angles. However, the comparison to the experimental results is hindered by the lack of adequate experimental data. Due to vibrations in the actuator plate, the experimental shear strain data could not be used. Hence, there are no experimental data to validate the post-failure behavior. Still, as shown above, the post-failure behavior was in agreement with results of other numerical studies (e.g., Mede et al., 2018).

We showed that the onset of failure corresponded to a strong increase in the number of broken bonds and in actuator layer acceleration. The maximum acceleration was reached towards the end of the softening phase. In fracture mechanics, the zone where softening occurs is generally referred to as the fracture process zone (FPZ) (Bazant and Planas, 1998). Hence, our findings suggest that slab acceleration may be used to accurately track the crack tip location in the weak layer during crack propagation experiments.

Introducing the softening ratio (R) showed that the stress decrease in softening only depends on particle modulus $E_{particle}$ and bond strength σ_{bond}^{th} , which allows estimating the maximum acceleration of the actuator layer and the damage dynamics. In the present formulation of our model, the softening ratio is fixed for a given pair of parameters ($E_{particle}$ and σ_{bond}^{th}).

To limit the number of model parameters we made two assumptions: the contact and the bond elastic modulus are equal and the bond cohesive and tensile strength are equal. The choice of weak layer creation technique (cohesive ballistic deposition) caused unique structural anisotropy that was reflected in the mechanical behaviour and added a limitation on the post-failure behavior and the shape of the failure envelope. Investigating the influence of microstructure by modifying the porosity or the coordination number as the sticky hard sphere (Gaume et al., 2017a) and/or modifying the assumption on contact/bond elastic modulus would allow us to generate a larger range of stress decrease during the softening phase.

Furthermore, in the future, the influence of the ratio between the bond tensile strength and the bond cohesive strength, and/or the weak layer microstructure on the yield surface might be explored.

The developed simulation tool does not take into account snow sintering processes, as we limited the study to fast loading rates. In the context of a dry-snow slab avalanche formation, this means that we can only study artificially induced cracks due to skiers or explosives. In future, we plan to extend the work to larger systems with the objective of studying the micromechanics of the dynamics of crack propagation. Using the presented tool to model a PST already showed some promising preliminary results (Bobillier et al., 2018).

39 Conclusions

15 Understanding the failure behaviour of slab and weak layer independently and characterize the influence of the main parameters is a prerequisite for studying the dynamics of crack propagation leading to the release of a dry-snow slab avalanche.

We developed a mesoscale (between snow grain and slope scale) simulation tool based on 3-D discrete element simulations to generate snow layers of varying properties and investigate micromechanical processes at play during snow failure. Two types of snow layers were generated by ballistic deposition technique: (1) a uniform snow slab and (2) a porous transversally isotropic weak snow layer. These two types of snow layers are the two main components of dry-snow slab avalanches. The layers were characterized by a linear relation between particle/contact parameters and macroscopic properties. By deliberately making the choice of not representing the real snow microstructure, the computational time decreases and allows creating relatively large systems.

We found an elastic-brittle mechanical behaviour for slab layers in tension. The weak layer behaviour under mixed-mode loading included four distinct phases of deformation (elastic, softening, simultaneous brittle crushing and shear displacement and finally shear displacement) as recently reported in the literature. The weak layer failure envelope, derived from a series of mixed-mode loading simulations under different loading angles, was in good agreement with previous experimental and numerical results. The closed-form failure envelope can be tuned by adjusting the bond strength parameter.

Analysing weak layer features such as the proportion of broken bonds, normal acceleration and softening ratio showed some of the limitations induced by our assumptions on particle parameters and the uniqueness of the microstructure generation. Still,

the validation results suggest that the presented simulation tool can reproduce the main behaviour of weak layers under mixed-mode loading conditions – even though we strongly simplified the microstructure to limit the computational costs.

In the future, we intend to increase the system size and simulate a propagation saw test and explore the dynamics of crack propagation that eventually leads to dry-snow slab avalanche release.

5 40 Acknowledgements

We thank the two anonymous reviewers and the Editor Evgeny A. Podolskiy for their constructive reviews that helped us to improve our manuscript.

41 References

- 10 Bair, E. H., Simenhois, R., van Herwijnen, A., and Birkeland, K.: The influence of edge effects on crack propagation in snow stability tests, *Cryosphere*, 8, 1407-1418, <https://doi.org/10.5194/tc-8-1407-2014>, 2014.
- Bazant, Z. P., and Planas, J.: *Fracture and size effect in concrete and other quasibrittle materials*, CRC Press, Boca Raton, U.S.A., 616 pp., 1998.
- 15 Bobillier, G., Gaume, J., van Herwijnen, A., Dual, J., and Schweizer, J.: Modeling the propagation saw test with discrete elements, *Proceedings ISSW 2018. International Snow Science Workshop, Innsbruck, Austria, 7-12 October 2018*, 976-980, 2018.
- Capelli, A., Reiweger, I., and Schweizer, J.: Acoustic emissions signatures prior to snow failure, *J. Glaciol.*, 64, 543-554 <https://doi.org/10.1017/jog.2018.43>, 2018.
- Cundall, P. A., and Strack, O. D. L.: A discrete numerical model for granular assemblies, *Geotechnique*, 29, 47-65, <https://doi.org/10.1680/geot.1979.29.1.47>, 1979.
- 20 Gaume, J., van Herwijnen, A., Chambon, G., Birkeland, K. W., and Schweizer, J.: Modeling of crack propagation in weak snowpack layers using the discrete element method, *Cryosphere*, 9, 1915-1932, <https://doi.org/10.5194/tc-9-1915-2015>, 2015.
- Gaume, J., Löwe, H., Tan, S., and Tsang, L.: Scaling laws for the mechanics of loose and cohesive granular materials based on Baxter's sticky hard spheres, *Phys. Rev. E*, 96, 032914, <https://doi.org/10.1103/PhysRevE.96.032914>, 2017a.
- 25 Gaume, J., van Herwijnen, A., Chambon, G., Wever, N., and Schweizer, J.: Snow fracture in relation to slab avalanche release: critical state for the onset of crack propagation, *Cryosphere*, 11, 217-228, <https://doi.org/10.5194/tc-11-217-2017>, 2017b.
- Gaume, J., Gast, T., Teran, J., van Herwijnen, A., and Jiang, C.: Dynamic anticrack propagation in snow, *Nat. Commun.*, 9, 3047, <https://doi.org/10.1038/s41467-018-05181-w>, 2018.
- 30 Gauthier, D., and Jamieson, J. B.: Towards a field test for fracture propagation propensity in weak snowpack layers, *J. Glaciol.*, 52, 164-168, <https://doi.org/10.3189/172756506781828962>, 2006.
- Gerling, B., Löwe, H., and van Herwijnen, A.: Measuring the elastic modulus of snow, *Geophys. Res. Lett.*, 44, 11088-11096, <https://doi.org/10.1002/2017GL075110>, 2017.
- 35 Gibson, L. J., and Ashby, M. F.: *Cellular Solids: structure and properties*, 2nd ed., Cambridge University Press, Cambridge, U.K., 510 pp., 1997.
- Hagenmuller, P., Theile, T. C., and Schneebeli, M.: Numerical simulation of microstructural damage and tensile strength of snow, *Geophys. Res. Lett.*, 41, 86-89, <https://doi.org/10.1002/2013gl058078>, 2014.

- Hagenmuller, P., Chambon, G., and Naaim, M.: Microstructure-based modeling of snow mechanics: a discrete element approach, *Cryosphere*, 9, 1969-1982, <https://doi.org/10.5194/tc-9-1969-2015>, 2015.
- Johnson, J. B., and Hopkins, M. A.: Identifying microstructural deformation mechanisms in snow using discrete-element modeling, *J. Glaciol.*, 51, 432-442, <https://doi.org/10.3189/172756505781829188>, 2005.
- 5 Kadam, D., and Herrmann, H. J.: Density profiles of loose and collapsed cohesive granular structures generated by ballistic deposition, *Phys. Rev. E*, 83, 031301, <https://doi.org/10.1103/PhysRevE.83.031301>, 2011.
- Ken-Ichi, K.: Distribution of directional data and fabric tensors, *International Journal of Engineering Science*, 22, 149-164, [https://doi.org/https://doi.org/10.1016/0020-7225\(84\)90090-9](https://doi.org/https://doi.org/10.1016/0020-7225(84)90090-9), 1984.
- 10 Löwe, H., Egli, L., Bartlett, S., Guala, M., and Manes, C.: On the evolution of the snow surface during snowfall, *Geophys. Res. Lett.*, 34, <https://doi.org/10.1029/2007GL031637>, 2007.
- McClung, D. M.: Shear fracture precipitated by strain softening as a mechanism of dry slab avalanche release, *J. Geophys. Res.*, 84, 3519-3526, <https://doi.org/10.1029/JB084iB07p03519>, 1979.
- Mede, T., Chambon, G., Hagenmuller, P., and Nicot, F.: Snow failure modes under mixed loading, *Geophys. Res. Lett.*, 45, <https://doi.org/10.1029/2018GL080637>, 2018.
- 15 Mulak, D., and Gaume, J.: Numerical investigation of the mixed-mode failure of snow, *Computational Particle Mechanics*, <https://doi.org/10.1007/s40571-019-00224-5>, 2019.
- Potyondy, D. O., and Cundall, P. A.: A bonded-particle model for rock, *Int. J. Rock Mech. Min.*, 41, 1329-1364, <https://doi.org/10.1016/j.ijrmms.2004.09.011>, 2004.
- Reiweger, I., Gaume, J., and Schweizer, J.: A new mixed-mode failure criterion for weak snowpack layers, *Geophys. Res. Lett.*, 42, 1427-1432, <https://doi.org/10.1002/2014GL062780>, 2015.
- 20 Reuter, B., Schweizer, J., and van Herwijnen, A.: A process-based approach to estimate point snow instability, *Cryosphere*, 9, 837-847, <https://doi.org/10.5194/tc-9-837-2015>, 2015.
- Reuter, B., and Schweizer, J.: Describing snow instability by failure initiation, crack propagation, and slab tensile support, *Geophys. Res. Lett.*, 45, 7019-7027, <https://doi.org/10.1029/2018GL078069>, 2018.
- 25 Schweizer, J., Jamieson, J. B., and Schneebeli, M.: Snow avalanche formation, *Rev. Geophys.*, 41, 1016, <https://doi.org/10.1029/2002RG000123>, 2003.
- Shertzer, R. H.: Fabric tensors and effective properties of granular materials with application to snow, Ph.D., Montana State University, Bozeman MT, U.S.A., 258 pp., 2011.
- Shertzer, R. H., Adams, E. E., and Schneebeli, M.: Anisotropic thermal conductivity model for dry snow, *Cold Reg. Sci. Technol.*, 67, 122-128, <https://doi.org/10.1016/j.coldregions.2011.09.005>, 2011.
- 30 Sigrist, C.: Measurement of fracture mechanical properties of snow and application to dry snow slab avalanche release, Department of Mechanical and Process Engineering, ETH Zurich, Zurich, Switzerland, 139 pp., 2006.
- Sigrist, C., and Schweizer, J.: Critical energy release rates of weak snowpack layers determined in field experiments, *Geophys. Res. Lett.*, 34, L03502, <https://doi.org/10.1029/2006GL028576>, 2007.
- 35 Srivastava, P. K., Chandel, C., Mahajan, P., and Pankaj, P.: Prediction of anisotropic elastic properties of snow from its microstructure, *Cold Reg. Sci. Technol.*, 125, 85-100, <https://doi.org/10.1016/j.coldregions.2016.02.002>, 2016.
- van Herwijnen, A., and Jamieson, B.: High-speed photography of fractures in weak snowpack layers, *Cold Reg. Sci. Technol.*, 43, 71-82, <https://doi.org/10.1016/j.coldregions.2005.05.005>, 2005.
- van Herwijnen, A., Schweizer, J., and Heierli, J.: Measurement of the deformation field associated with fracture propagation in weak snowpack layers, *J. Geophys. Res.*, 115, F03042, <https://doi.org/10.1029/2009JF001515>, 2010.
- 40 van Herwijnen, A., Gaume, J., Bair, E. H., Reuter, B., Birkeland, K. W., and Schweizer, J.: Estimating the effective elastic modulus and specific fracture energy of snowpack layers from field experiments, *J. Glaciol.*, 62, 997-1007, <https://doi.org/10.1017/jog.2016.90>, 2016.

Table 1: Mechanical properties used for simulation.

Mechanical property	Macroscopic	Particles
Weak layer density (kg m ⁻³)	110	550
Slab layer density (kg m ⁻³)	250	455
Slab porosity	45%	-
Weak layer porosity	80%	-
Slab elastic modulus	0.7 – 5.5 MPa	1 – 10.5 MPa
Weak layer elastic modulus	0.5 – 7 MPa	40 – 480 MPa
Slab strength	5 – 18 kPa	6 – 19 kPa
Weak layer strength	1 – 9 kPa	70 – 560 kPa

Table 2: Characteristics of the three cold laboratory experiments used for model validation.

Characteristics	Experiment		
	1	2	3
Base layer density (kg m ⁻³)	392	271	289.5
Weak layer density (kg m ⁻³)	174	170	170
Slab layer density (kg m ⁻³)	399	212	293
Base layer main type of grain	Faceted crystals	Faceted crystals	Faceted crystals
Weak layer main type of grain	Depth hoar	Depth hoar	Depth hoar
Slab layer main type of grain	Faceted crystals	Faceted crystals	Faceted crystals
Base layer, size of grain (mm)	0.7-1.5-2	1-2	1-1.5
Weak layer, size of grain (mm)	2-4	2-4	3-4
Slab layer, size of grain (mm)	0.7-1.5	1-2	1-1.5
Failure stress (kPa)	10.5	3.2	8.3

Failure strain	0.0019	0.00243	0.00198
Loading rate stress (Pa s ⁻¹)	168	168	168
Loading angle (°)	0	15	35

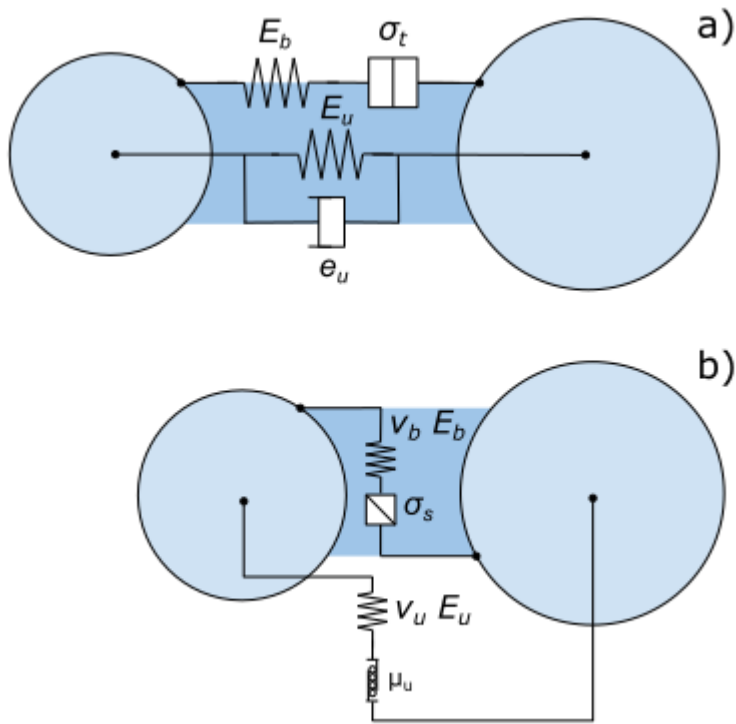


Figure 18: Representation of the PFC parallel bond model (PBM) used in the simulations. a) Normal mechanical parameter bond and unbonded, where E_b represents the bond elastic modulus, σ_t the tensile strength, E_u the contact elastic modulus and e_u the restitution coefficient. b) Shear mechanical parameter bond and unbonded, where E_b represents the bond elastic modulus, σ_s the shear strength, E_u the contact elastic modulus, ν_b the bond Poisson's ratio and μ_u the friction coefficient.

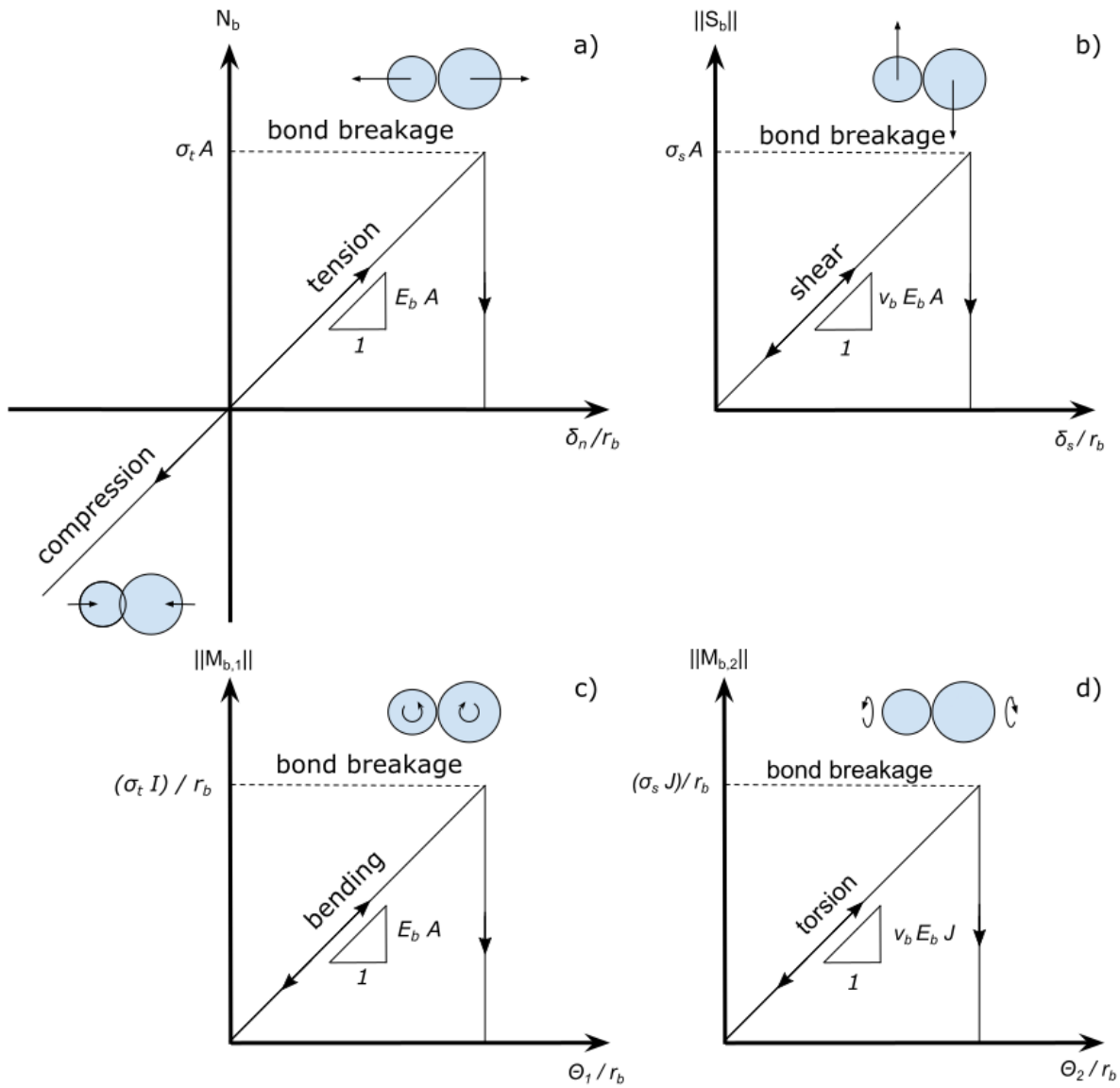
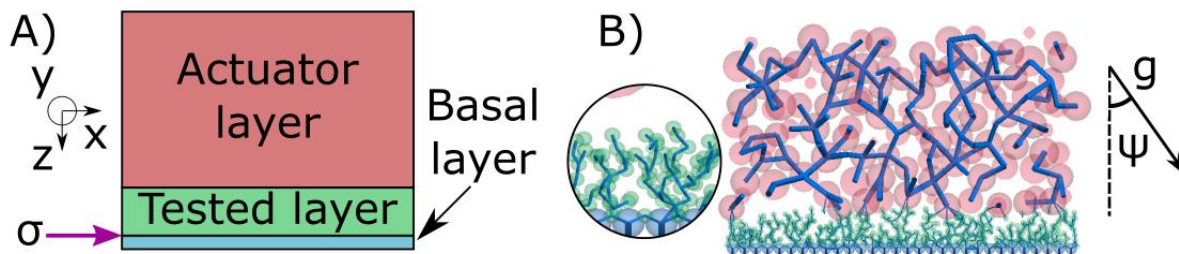
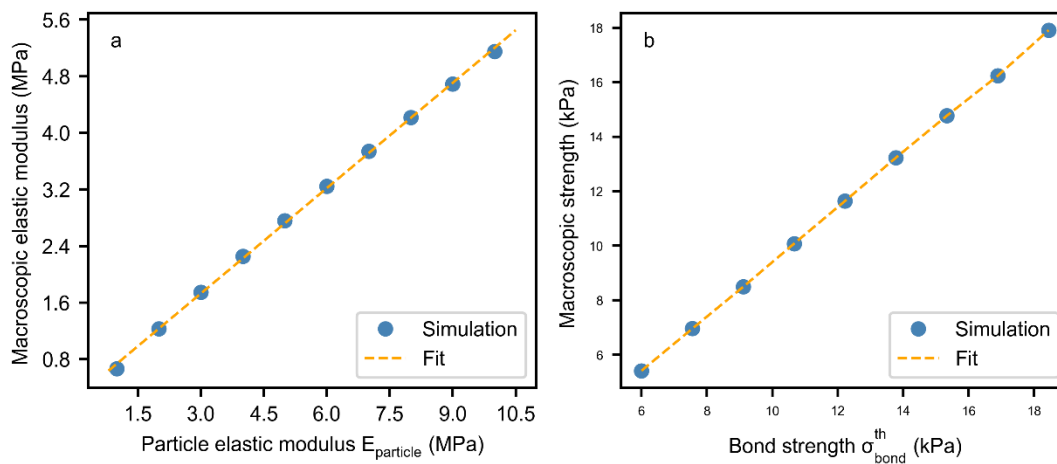


Figure 19: Representation of the bonded behavior of PBM used in the simulations. (a) Bond normal force N_b as a function of the normal interpenetration δ_n scaled by the bond radius r_b . (b) Bond shear force $\|S_b\|$ as a function of tangential interpenetration δ_s scaled by the bond radius r_b . (c) Bond-bending moment $\|M_{b,1}\|$ as a function of bending rotation θ_1 scaled by the bond radius r_b . (d) Torsion moment $\|M_{b,2}\|$ as a function of twist rotation θ_2 scaled by the bond radius r_b .

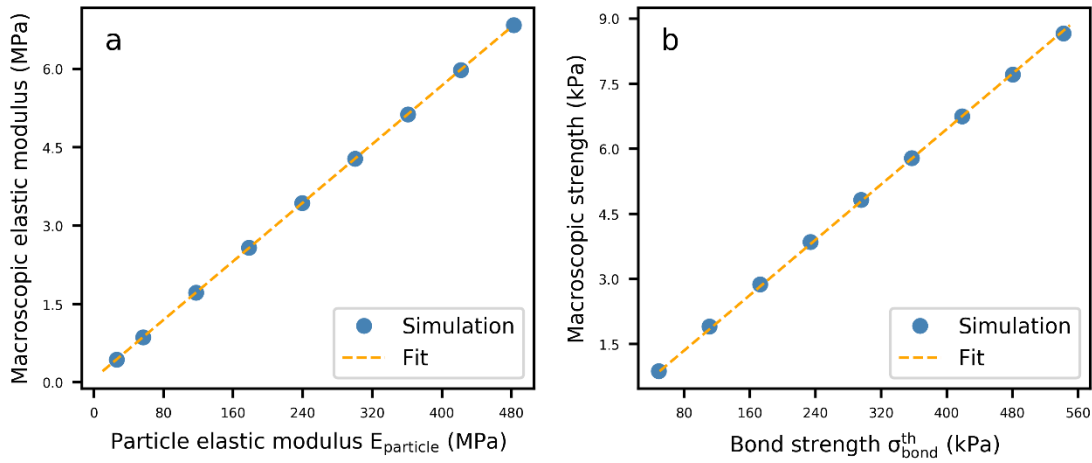
5



5 Figure 20: A) Coordinate system and diagram of the setup consisting of the basal layer (blue), the tested layer, in this case a weak layer, (green) and the actuator layer (red). The violet arrow points to the interface between basal and tested layer where the stress is measured. B) slice of a generated system consisting of a slab layer (large red particles) and a porous weak layer (small green particles). A zoom of the weak layer is shown in the circle. The lines represent bonds between particles. Applied gravity is defined on the right where ψ is the loading angle.



10 Figure 21: (a) Slab macroscopic elastic modulus as a function of particles elastic modulus. The blue dots correspond to the mean of ten simulations with different values of σ_{bond}^{th} . (b) Slab macroscopic strength as a function of slab particles strength obtained with unconfined load-controlled compression simulations. The blue dots correspond to the mean of ten simulations with different values of $E_{particle}$.



5 **Figure 22: (a) Weak layer macroscopic elastic modulus as a function of particles elastic modulus. The blue dots correspond to the mean of nine simulations with different values of σ_{bond}^{th} . (b) Weak layer macroscopic strength as a function of slab particles strength obtained with unconfined load-controlled compression simulations. The blue dots correspond to the mean of nine simulations with different values of $E_{particle}$.**

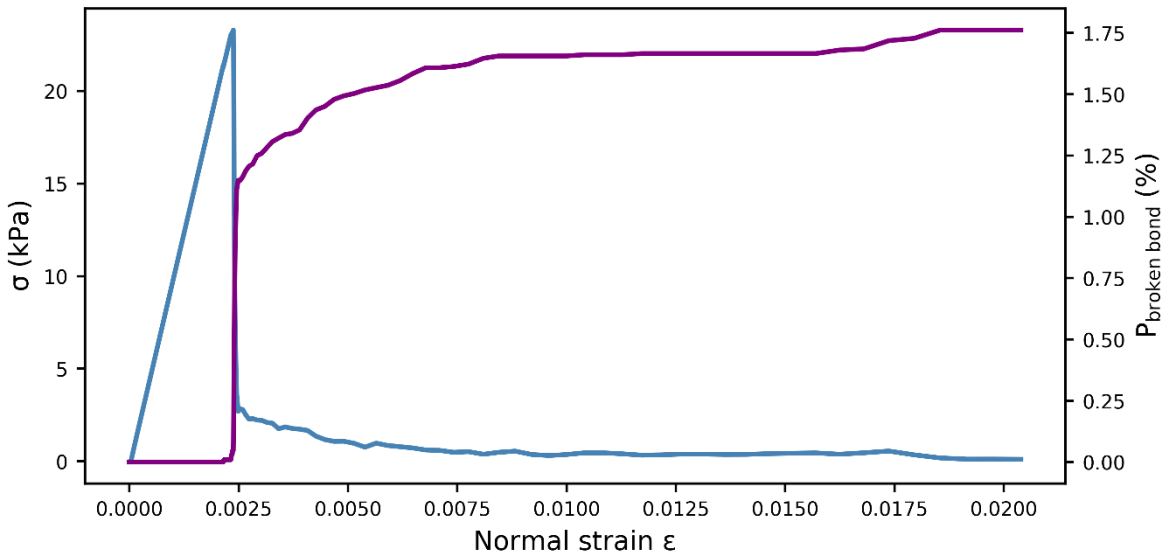


Figure 23: Slab layer behavior under load-controlled tension test. The blue line shows the normal stress, the violet line corresponds to the bond breaking ratio are shown as functions of the normal strain.

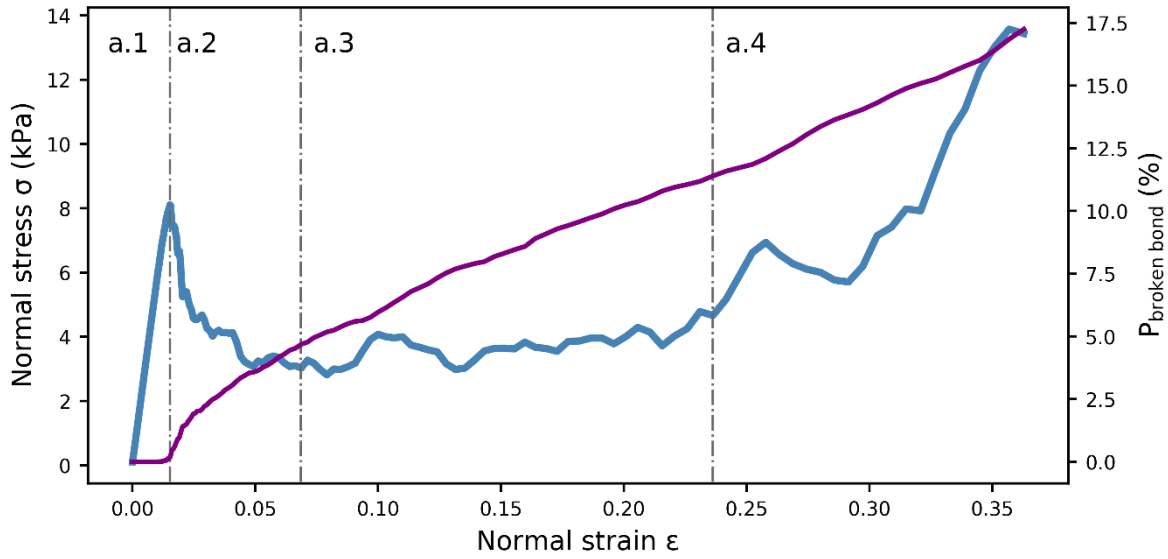


Figure 24: Weak layer behavior under load-controlled compression test ($E_{particle} = 30MPa$ and $\sigma_{bond}^{th} = 500kPa$). The blue line shows the normal stress during the four phases of weak layer failure. It includes the linear elastic phase (a.1), softening (a.2), brittle crushing (a.3), densification (a.4). The violet line corresponds to the proportion of broken bonds.

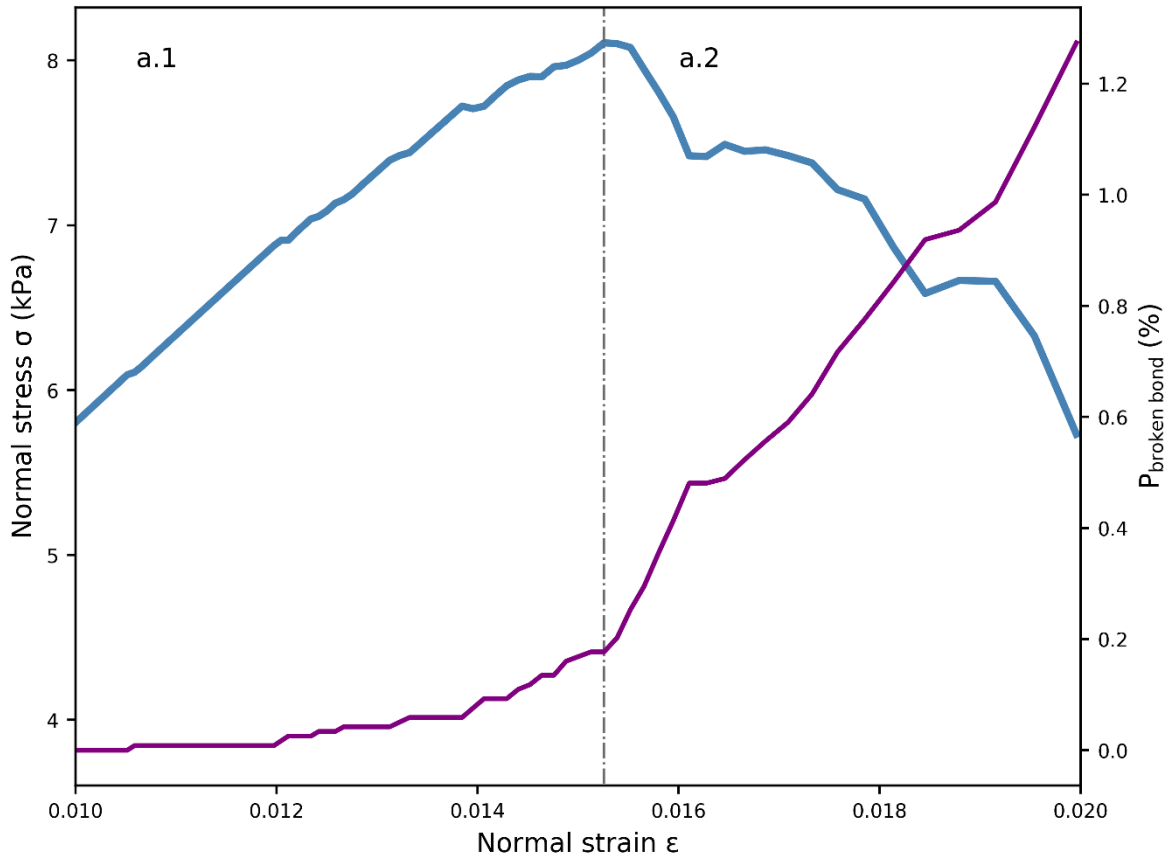


Figure 25: Weak layer behaviour close to failure under load-controlled compression ($E_{particle} = 30$ MPa and $\sigma_{bond}^{th} = 500$ kPa. The blue line shows the normal stress during the two first phases of weak layer failure. It includes the elastic (a.1) and the softening phase (a.2). The violet line corresponds to the proportion of broken bonds.

5

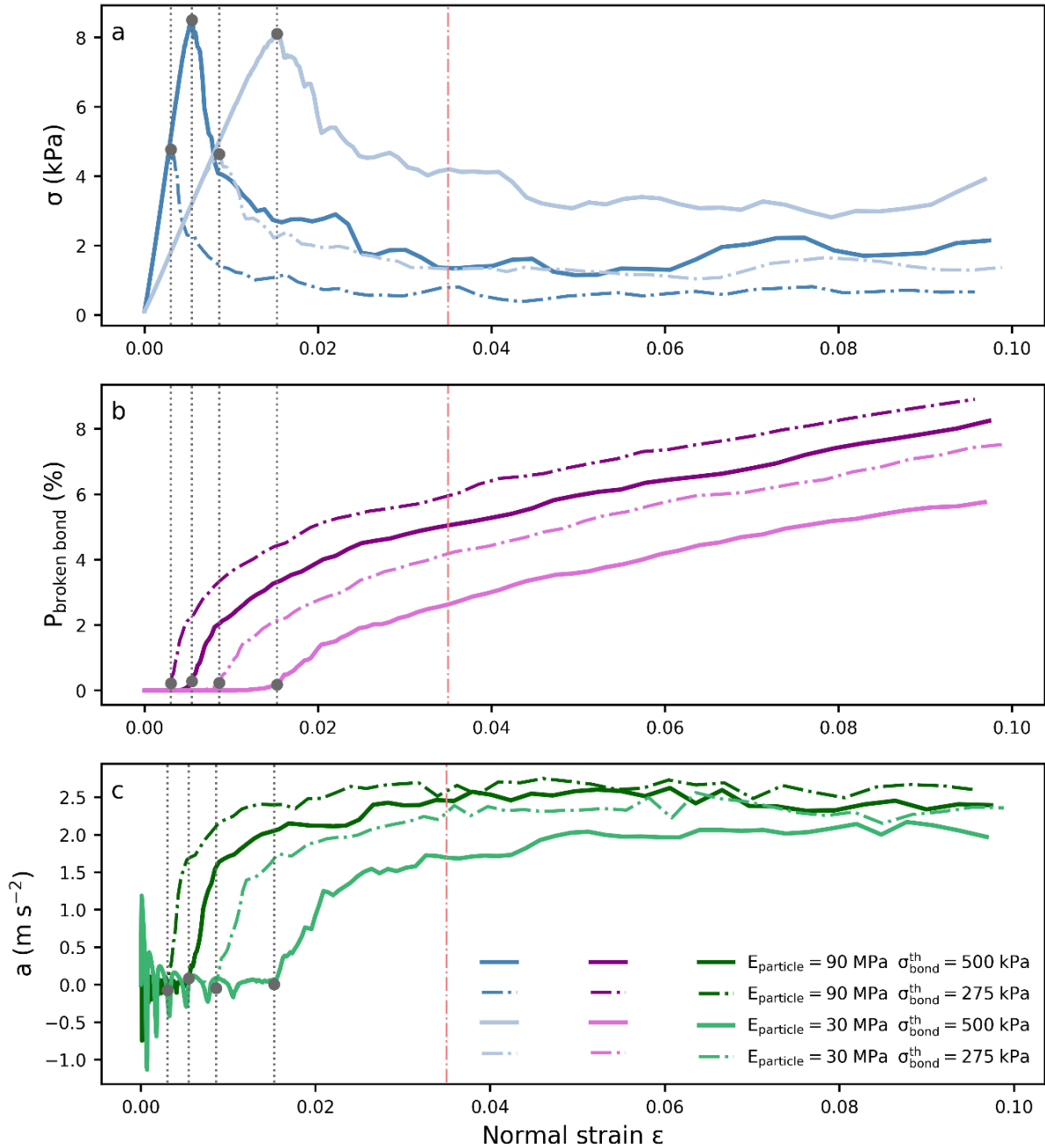


Figure 26: Weak layer behavior under load-controlled compression for four combinations of E_{particle} (solid lines) and $\sigma_{\text{bond}}^{\text{th}}$ (same color, dashed-dotted lines). (a) Normal stress vs. normal strain. (b) Percentage of broken bonds (damage). (c) Acceleration of the actuator layer. The orange dashed-dotted line represents the approximate beginning of the brittle crushing phase. The grey dotted line represents the beginning of the softening phase defined by the strength (grey dot).

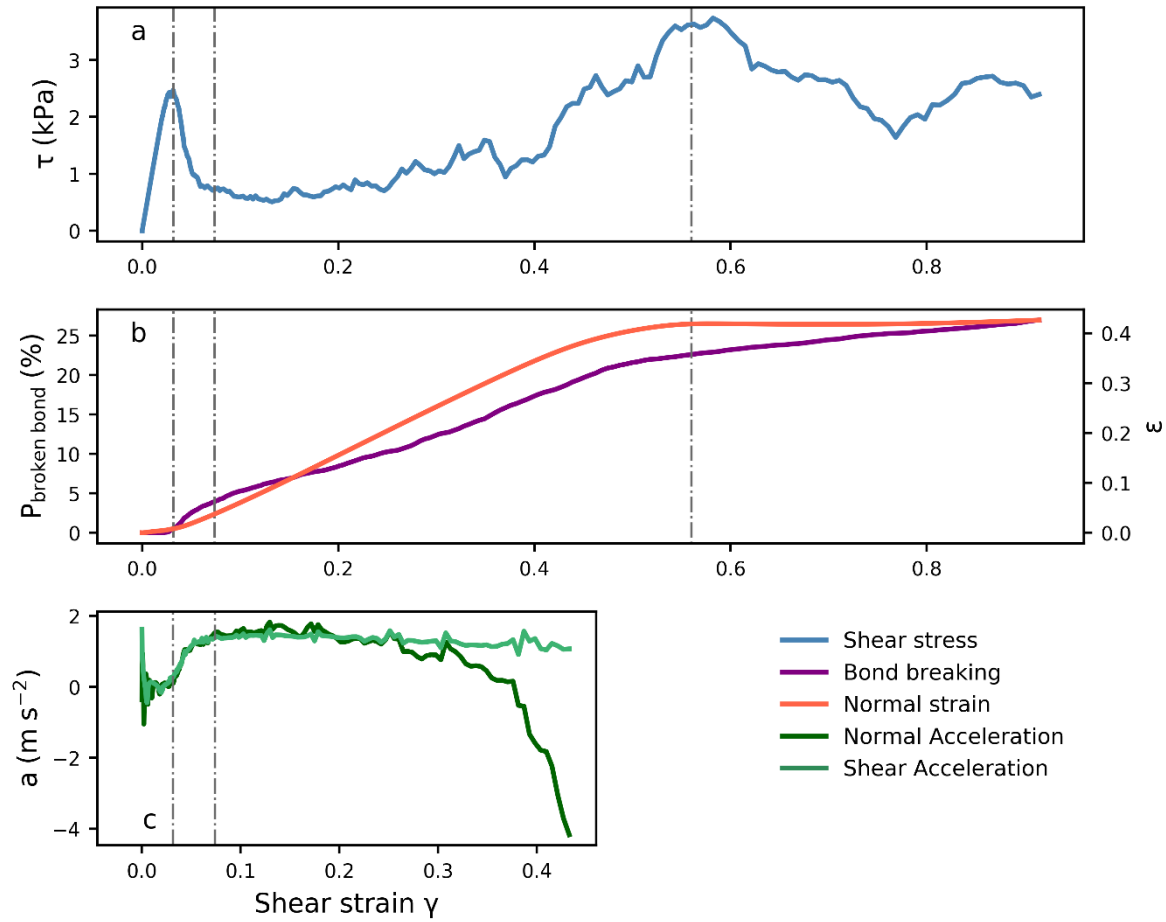
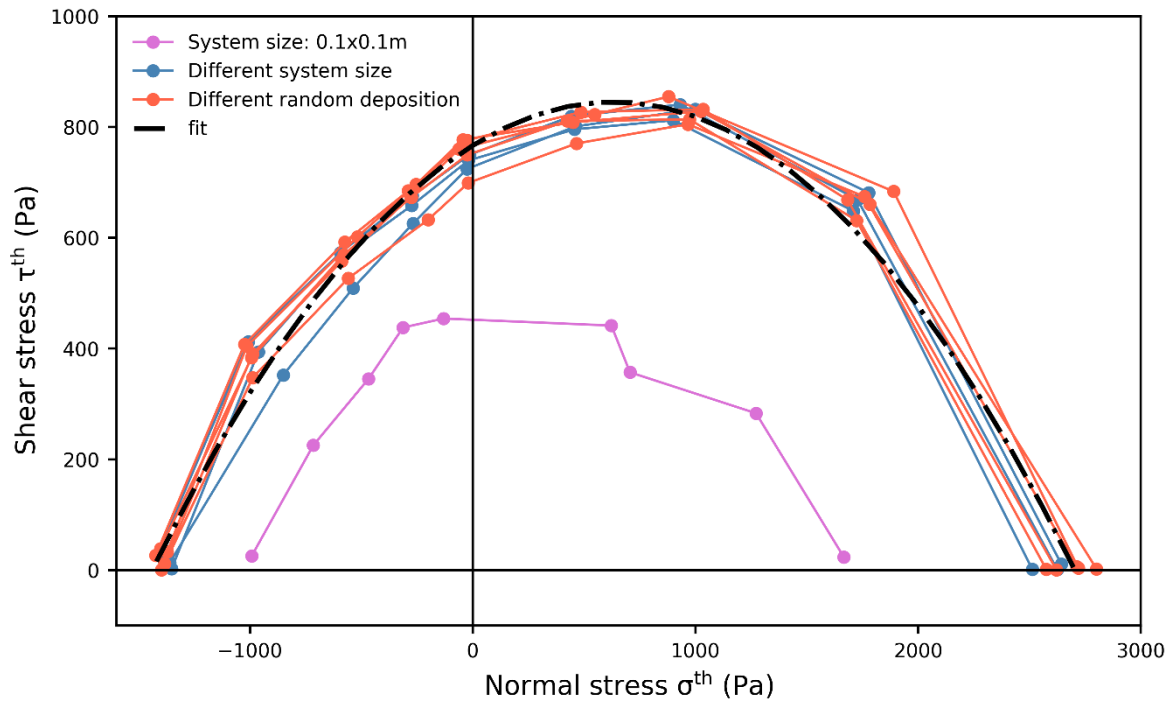


Figure 27: Weak layer behavior in load-controlled mixed-mode testing at 35° from the horizontal ($E_{\text{particle}} = 30\text{MPa}$ and $\sigma_{\text{bond}}^{\text{th}} = 500\text{kPa}$). (a) Shear stress, (b) bond damage (violet) and normal strain (orange, right scale), and (c) normal and tangential accelerations are shown as function of the shear strain.



5 **Figure 28:** Failure envelopes for different sample sizes, and types of random particle deposition. The blue lines correspond to different sample sizes from $0.3 \text{ m} \times 0.3 \text{ m}$ to $0.6 \text{ m} \times 1 \text{ m}$. The pink line corresponds to a sample size of $0.1 \text{ m} \times 0.1 \text{ m}$. The orange lines correspond to a sample size of $0.3 \text{ m} \times 0.3 \text{ m}$ generated with different random depositions. The black dash-dotted line corresponds to a 2nd order polynomial fit of all data apart from those obtained with the sample size of $0.1 \text{ m} \times 0.1 \text{ m}$.

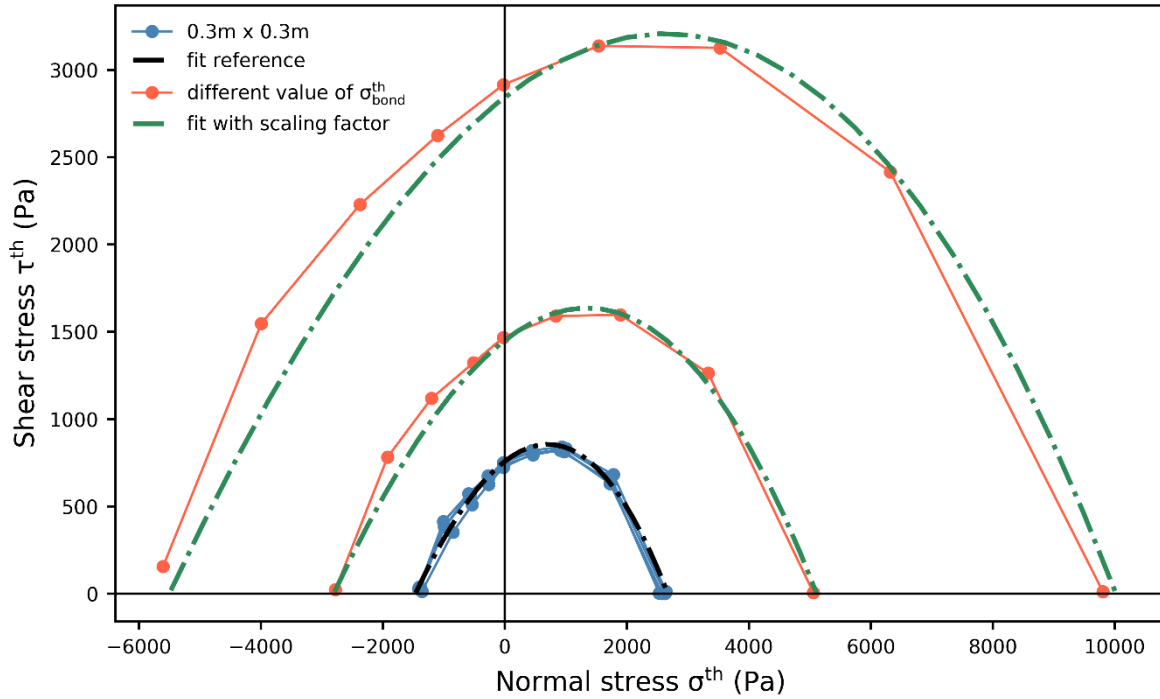


Figure 29: Failure envelopes for different values of bond strength σ_{bond}^{th} and fit only based on equation (10). The blue lines correspond to the data shown in Figure 28 and the black dash-dotted line to the corresponding fit (Eq. 8). The orange lines correspond to failure envelopes with different values of bond strength σ_{bond}^{th} . The green dash-dotted line corresponds to the corresponding fit defined in equation (10) which do not depend on orange line data.

5

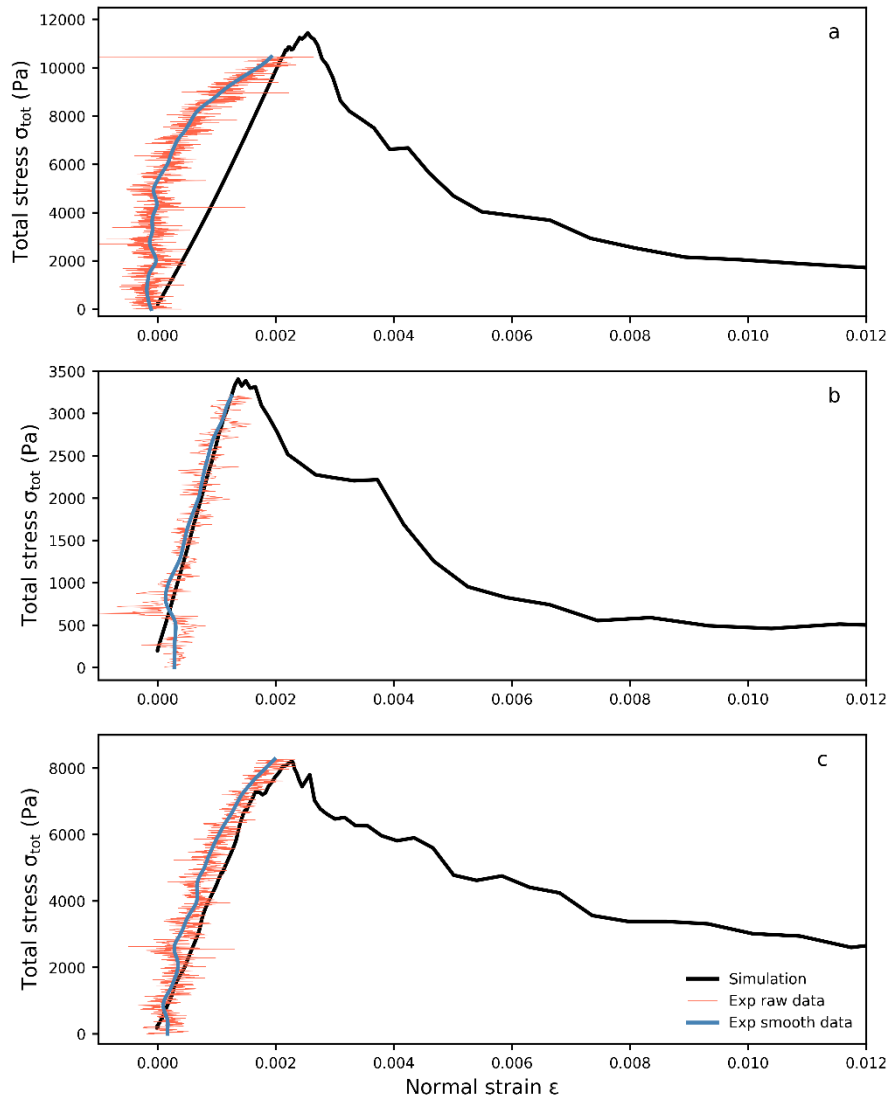


Figure 30: Total stress as function of normal strain for three simulations and the corresponding experimental results. (a) for a loading angle of 0° , (b) 15° and (c) 35° . The orange lines shows the raw stress data, the blue lines are the smoothed stress using a Kalman filter (Capelli et al., 2018) and the black lines are the simulation results.